Direct Observation of Polaritonic Chemistry by Nuclear Magnetic Resonance Spectroscopy

B. Patrahau[§], M. Piejko[§], R. Mayer, C. Antheaume, T. Sangchai, G. Ragazzon, A. Jayachandran, E. Devaux, C. Genet, J. Moran*, T.W. Ebbesen*

[§] Equal contribution

University of Strasbourg, CNRS, ISIS & icFRC, 8 allée Gaspard Monge, 67000 Strasbourg, France

ABSTRACT

Polaritonic chemistry is emerging as a powerful approach to modifying the properties and reactivity of molecules and materials. However, probing how the electronics and dynamics of molecular systems change under strong coupling has been challenging due to the narrow range of spectroscopic techniques that can be applied *in situ*. Here we develop microfluidic optical cavities for vibrational strong coupling (VSC) that are compatible with nuclear magnetic resonance (NMR) spectroscopy using standard liquid NMR tubes. VSC is shown to influence the equilibrium between two conformations of a molecular balance sensitive to dispersion forces, revealing a clear change in the equilibrium constant under VSC. In all compounds studied, VSC does not induce detectable changes in chemical shifts, J-couplings, or spin-lattice relaxation times. This unexpected finding indicates that VSC does not substantially affect molecular electron density distributions, and in turn has profound implications for the possible mechanisms at play in polaritonic chemistry under VSC and suggests that the emergence of collective behavior is critical.

INTRODUCTION

Vibrational strong light-matter coupling (VSC) has emerged as an innovative approach for influencing molecular properties and chemical reactivity *(1,2)*. In VSC, molecular vibrational transitions are strongly coupled to the zero-point electromagnetic fluctuations of an infrared cavity. Under the right conditions, this interaction gives rise to two hybrid light-matter vibropolaritonic states (VP+ and VP-) along with N-1 dark collective states (DS) resulting from the coupling of N molecules with the optical mode. The formation of these hybrid states, which occurs in the dark, has been shown to alter reaction rates *(3–10),* chemical selectivity *(11–13),* electrochemical modulation *(14),* charge transfer equilibria *(15)* and many other properties such as ionic conductivity *(16,17),* electrical conductivity *(18),* solvent polarity *(19),* crystallization *(20)* or self-assembly *(21,22)*.

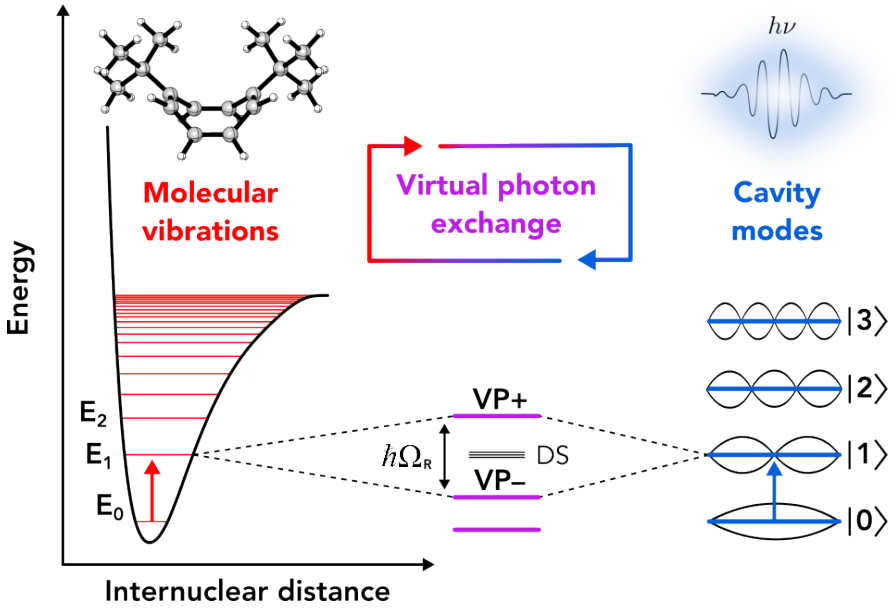

Figure 1. Schematic diagram of the formation of vibro-polaritonic states. VP+ and VP– are the upper and lower bright vibropolaritonic states and DS degenerate dark states from resonant vibrational and optical transitions.

Despite the numerous experimental studies of chemistry and properties under VSC *(1–27)* and extensive theoretical studies *(28–41),* a detailed understanding of the underlying processes is still lacking. Systematic experimental studies on a variety of molecular systems should help to constrain the different models and to extract general principles for how VSC influences chemistry. However, such experiments are challenging because existing setups are not easily compatible with real-time spectroscopic monitoring. The cavities used for VSC are typically composed of two parallel mirrors (Fabry-Perot resonators) that are tuned at normal

incidence ($k_{//}$=0) by compressing a polymer spacer which, in turn, deforms the mirrors. The resulting cavity is therefore tuned only within a small sweet spot through which spectroscopic analysis must be carried out. In addition, the high reflectivity of the mirrors complicates spectroscopy in the IR and UV-Vis regions. Taken together, these aspects make it difficult to experimentally probe how VSC influences chemistry, impact the reproducibility of VSC studies, and constitute barriers to entry for scientists unfamiliar with optics.

In response to these challenges, we have developed a new type of Fabry-Perot (FP) cavity in a microfluidic chip designated for vibrational strong coupling that can be used easily by non-specialists (Fig. 2). These cavities are compatible not only with the previously used spectroscopic methods, but most importantly the chemistry can be directly monitored by standard liquid Nuclear Magnetic Resonance (NMR) spectroscopy following a protocol we have developed for this purpose. This gives VSC experiments access to the full power of NMR spectroscopy, currently the most important and widely used technique in chemistry, enabling a direct and detailed characterization of a broad range of chemical and biological systems. These cavities ensure that the entire volume can be strongly coupled and are available in a set of different fixed path lengths, each one resonating at different frequencies - like piano keys. Since tuning is no longer required their use is simplified and the reproducibility of the measurement should increase.

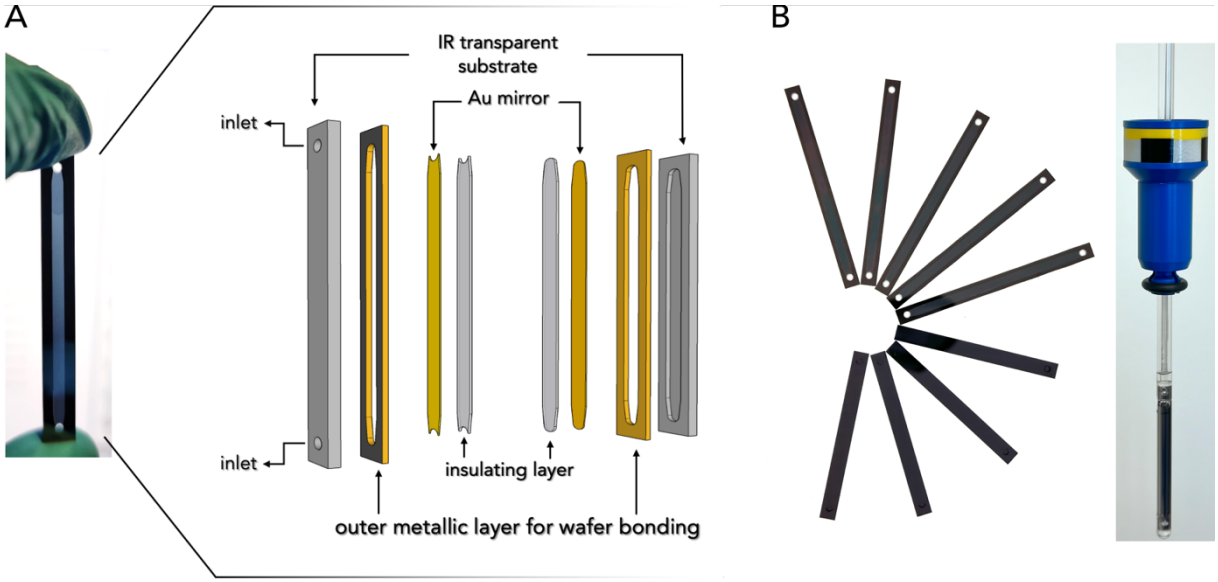

Figure 2. Microfluidic cavities compatible with NMR spectroscopy. (**A**) Photograph of a cavity being filled with liquid along with its cross section. (**B**) A set of NMR compatible cavities of different pathlengths and an NMR tube containing a sealed cavity immersed in deuterated water and plastic holders used to center the cavity inside the tube.

The potential of these new NMR compatible cavities is illustrated by direct observation of the VSC-induced modification of intramolecular dispersion forces in a molecular balance which intercoverts between two conformations at thermodynamic equilibrium. Importantly, the NMR spectra of this compound, and a variety of others, under VSC show surprisingly that the chemical shifts, the J-couplings, and the spin-lattice relaxation time (T_1) remain unchanged under VSC. These observations enabled by the new cavities give insight into the mechanism of VSC and indicate that redistribution of electronic density is not the major cause of changes in chemical reactivity, solvent polarity, and molecular assembly under VSC.

At the outset of the cavity design, it was not clear whether NMR signals could be measured inside a microfluidic FP cavity. After all, a typical FP cavity formed with metallic gold mirrors separated by 10 μm might be a Faraday cage for the 500 MHz (0.6 m) frequency used to probe nuclei in a standard NMR spectrometer. To facilitate the measurements and allow for widespread adoption of the technique, the cavities should fit inside a standard tube normally used for liquid NMR spectroscopy (⌀ 5 mm). Additionally the FP cavity should have the same resonance wavelength everywhere across the microfluidic channel. To meet these requirements, we co-developed these FP cavities with Lion*iX* International, a specialized manufacturer of microsystems. After several iterations, the FP cavities were made in both fused silica and in Si substrates as they each have their distinct advantages. The former is transparent in the UV and visible region, but opaque below 2000 cm^{-1} while the latter is opaque across the UV-Vis, but transparent across the IR region of interest down to 500 cm^{-1}. Fig. 2A shows the cross-section and a photograph of a typical NMR-compatible FP cavity. Channels ~10 μm deep were etched into the substrate of choice, followed by deposition of 5 nm of Cr and 10 nm Au. To bond the top mirror to the bottom substrate bearing the channel, 200 nm Au was deposited on the substrate surface and the two parts were press-welded. The channel is 4 cm long, but only 2 mm wide to ensure flatness across the width. IR spectroscopy shows that the resonance varies by less than 3 cm^{-1} for a mode at 3038 cm^{-1}, implying that the path length is essentially constant everywhere in the channel (see SI for spectra and details). In the case of the cavities prepared in Si substrates, a SiO_x layer (100 nm) was also added to protect the Au mirrors from reactive agents. The IR spectrum of a given cavity is shown in Fig. S5, with full width at half max (FWHM) around 80 cm^{-1} and Q factors of ~10. The cavities based on silica substrates can be characterized in the UV-Vis for changes in absorbance or fluorescence. Angular dispersion curves can easily be recorded, since the new cavity geometry does not hinder the light passing through the sample in a wide angle.

For NMR measurements, the following protocol must be followed to collect correct signals. The cavity must be centered in the NMR tube using a 3D-printed holder to ensure proper shimming (magnetic field homogeneity). Proper shimming is probably the most challenging step. The scarce amount of intracavity material (less than 2 μL of solution) makes it impossible to properly lock on to the NMR signal, and so the cavity is immersed in deuterated solvent, such as D_2O, which may additionally contain an external standard (*e.g.* dimethyl sulfone). To avoid any interaction with the outer deuterated solvent the holes used to insert the compound into the cavity must be sealed before introducing the cavity in the NMR tube. Furthermore, it became quickly clear that orientation of the cavity inside the spectrometer is also critical, and a long plastic holder was fabricated to ensure that the cavity is normal to the probe field (see SI). To enhance the low intensity of intracavity signals various solvent suppression pulse sequences can be used.

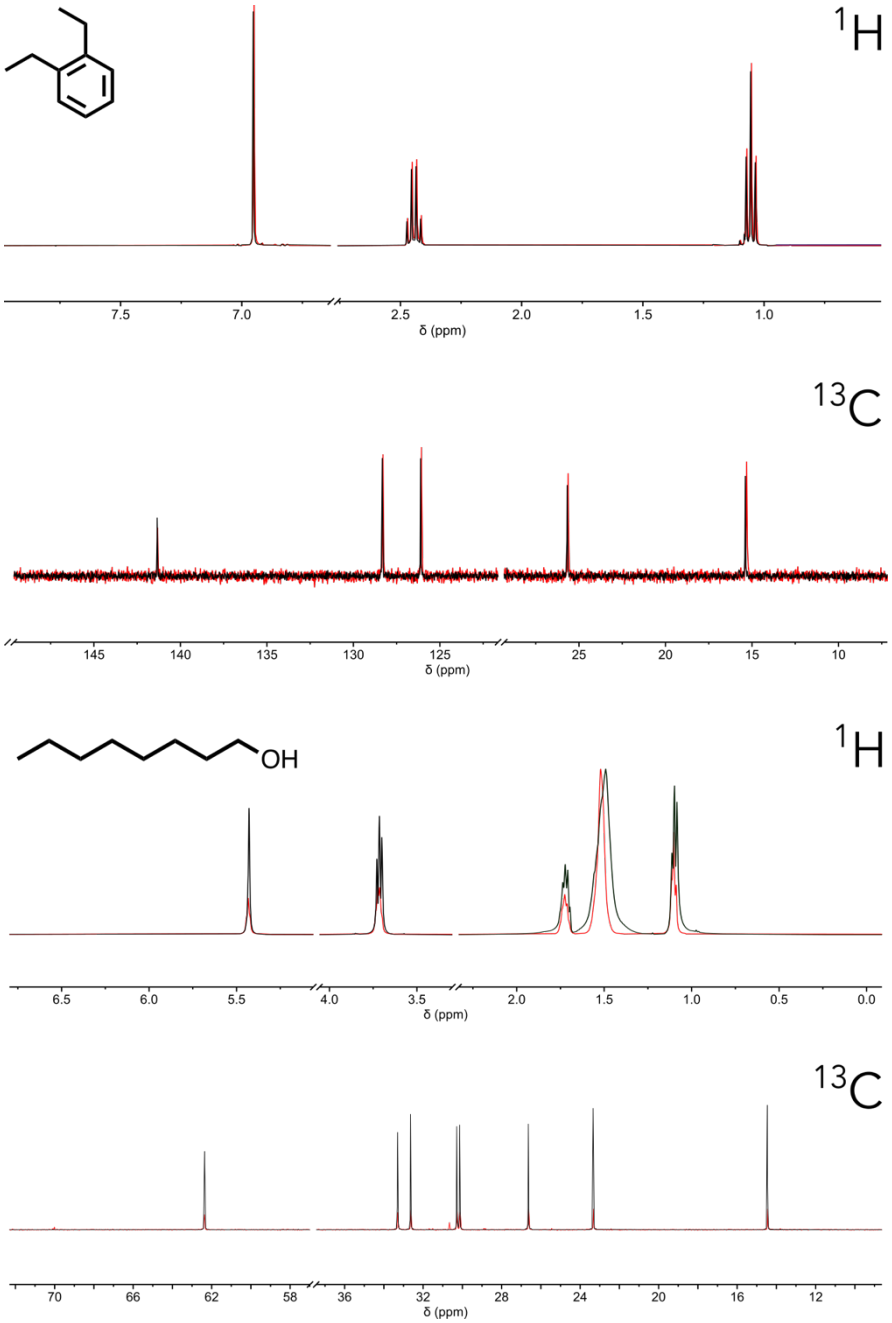

Figure 3. ^{1}H and ^{13}C NMR spectra of solvents. (**A**) 1,2-diethylbenzene and (**B**) octanol in an insert tube (black) and in a cavity (red) under VSC.

Fig. 3 shows the ^{1}H NMR and ^{13}C NMR spectra of 1,2–diethylbenzene and octanol recorded in a standard NMR tube containing just the solution or the solution in a FP cavity under VSC. Despite the potential challenges already discussed, a good quality signal can be obtained in the FP cavity.

Perhaps most surprisingly, when the different vibrational bands of these molecules are strongly coupled to the cavity mode, no changes in chemical shifts are detected by ^{1}H NMR

and ^{13}C NMR, the latter being much more sensitive to electron density changes. This observation holds for all other compounds and solvents that have thus far been tested. The absence of changes in chemical shift within experimental error under VSC is especially notable for octanol, since it undergoes a large change in polarity under VSC as detected with polarity sensitive Reichardt's dye *(19)*. Since ^{19}F NMR is even more sensitive than ^{13}C NMR, we also tested 1*H*,1*H*-tridecafluoro-1-heptanol with the OH stretcting mode under VSC but again any changes are within the experimental error. This implies that the electron density redistribution caused by VSC must be on average very small, to the point of being undetectable by NMR and is thus unlikely to be responsible for the observed changes in octanol polarity under VSC. Similarly, the fine structure coupling constant and spin-lattice relaxation time remain unchanged under VSC (see SI). These findings are very significant in that they narrow the possible explanations as to why VSC induces changes in chemical processes as will be discussed further down.

To prove the potential of NMR spectroscopy as a technique of choice for polaritonic chemistry, the developed NMR compatible cavities are used to directly probe the VSC-induced modification of dispersion forces. For this purpose, we set out to study the conformational equilibrium of a molecular balance (**1**), an established system for studying dispersion forces in solution (*42*) **1** consists of a cyclooctatetraene core bearing two *tert*-butyl moieties and exists in two conformations in which the *tert*-butyl groups are oriented towards or away from one another (named *folded* and *unfolded*, respectively – see Fig. 4). As demonstrated by Schreiner *et al*. (*42*), the folded conformer is stabilized by London dispersion forces between the two *tert*-butyl groups. In contrast, the *tert*-butyl groups are too far away from each other in the unfolded conformer to interact in an intramolecular fashion. The fact that the balance does not have any polarized functional groups, but instead is purely hydrocarbon-based is advantageous since it simplifies the behavior of the system as well as data interpretation.

To study the effect of VSC on the mentioned equilibrium, we synthesized this molecular balance and compared the equilibrium constant of the molecular balance in solutions of varying concentration in deuterated benzene. The equilibrium constant is measured by directly integrating signals in the quantitatively measured ^{1}H NMR spectrum:

$$K = \frac{C_{folded}}{C_{unfolded}} = \frac{\int folded}{\int unfolded}$$

where C_{folded}, $C_{unfolded}$ are the concentration of the folded and unfolded conformers and $\int folded$, $\int unfolded$ are the peak areas of the integrated intensity of both conformers respectively.

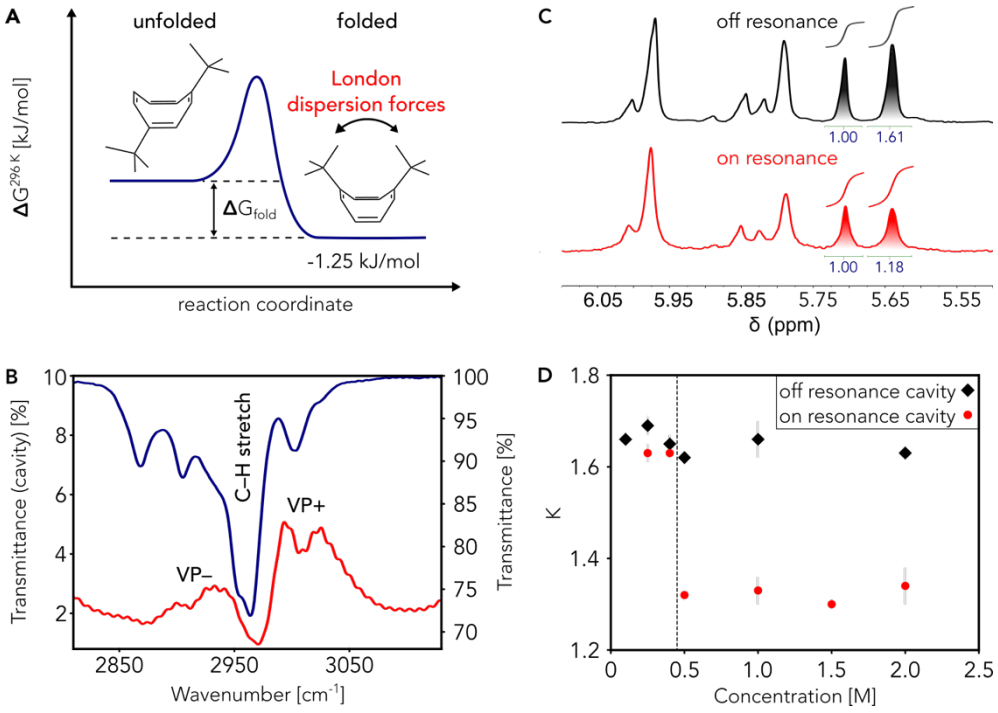

Figure 4. Influence of VSC on the London dispersion forces-driven equilibrium. (**A**) The cycloocatetraene-based molecular balance (**1**) exists in two distinct conformations (unfolded and folded). The ΔG_{fold} value corresponds to a solution of the molecular balance in benzene-d_6. (**B**) FT-IR spectrum of the neat molecular balance measured by ATR (navy blue) and a transmission-mode spectrum of a 1M solution of the molecular balance in benzene-d_6 in a cavity resonant with the C–H stretching mode at 2970 cm^{-1} showing the formation of two vibropolaritonic bands (VP– and VP+). (**C**) Partial ^1H NMR spectra in benzene-d_6 of the molecular balance in an off-resonance (black) or on-resonance (red) cavity. The shaded peaks originate from the same ^1H in the two different conformations (**D**) The concentration profile of the equilibrium constant (K) of the molecular balance in benzene-d_6 in cavities which are off and on resonance with the C–H stretching vibration (black and red datapoints, respectively). The error bars correspond to standard error.

First, we studied the equilibrium at low concentration (100 mM in benzene-d_6) in a standard NMR tube insert at 22 ± 1°C. The determined value of the equilibrium constant is in agreement with the data reported in the original study (1.67 ± 0.01) and corresponds to ΔG_{fold} = -1.25 kJ/mol. Next, cavities with two different path lengths were chosen that are either off-

resonance or on-resonance with the C-H stretching band of the molecular balance at 2970 cm^{-1}. It is important to note that strong coupling in the on-resonant cavities can only be reached above a certain concentration threshold when the concentration is sufficient to ensure that the exchange of virtual photons between the cavity mode and the molecules is faster than any dissipative process *(1,2).* In the off-resonance scenario, by increasing the concentration by up to 2 M, no change in the value of the equilibrium constant was observed. The value was identical (within experimental error) in the case of the on-resonance cavity at low concentration when there is still no strong coupling. However, at 0.5 M and upon reaching strong coupling condition, the equilibrium constant decreased sharply to a value of 1.33 ± 0.01, which corresponds to ΔG_{fold} = -0.70 kJ/mol. Interestingly, the value remained constant in solutions of higher concentration (up to 2 M). This phase transition-like behavior (Fig. 4D) indicates collective effects and is similar to the ones described in our previous work *(15,19).*

The behavior of the molecular balance is direct evidence that VSC alters London dispersion forces and confirms our suggestions inferred previous experiments as well as theoretical predictions *(43,44)* and other indirectly related experimental studies *(23).* The VSC-induced reduction of the equilibrium constant, and therefore, smaller Gibbs free energy difference between the two conformers implies that intramolecular dispersion forces are weaker under strong coupling. Outside cavity conditions, it is reported that the solvent reorganization entropy affects the dispersion interactions in the studied molecule whereas the dispersion enthalpy remains constant upon changing the solvent. The modification of solvent properties under VSC *(14,22)* might therefore derive from changes to solvation entropy due to N-1 dark states which appear when N molecules are coupled to a given optical mode *(45),* as in these experiments. The details of the various contributions are beyond this study and would benefit from further theoretical analysis.

It should be noted that again in studying the molecular balance, no changes in chemical shifts are observed under VSC despite the modification of the chemical equilibrium and the dispersion forces. More generally, considering the large effects of VSC on chemical reactivity, solvent polarity, aggregation, etc. significant chemical shift would naturally be expected. Afterall, a change in chemical reactivity, induced for example by functionalization, is typically associated with a change in electron density distribution in the reactant molecule which then shows up in the chemical shifts. The fact that it does not, implies that are factors are at play, in particular the emergence of collective behavior under VSC.

A chemical reactivity landscape is a multidimensional space along the various possible nuclear coordinates. Reactions proceed via the lowest energy coordinate which typically involves coupling between a vibrational mode and the electronic manifold (*i.e.,* vibronic coupling). Chemical reactivity changes observed under VSC are very sensitive to the symmetry of the vibrations that are strongly coupled because vibronic coupling is itself very sensitive to symmetry *(15)*. Upon VSC, the hybrid vibropolaritonic mode has a different symmetry than the bare vibration and thereby affects the normal pathway. If the low energy pathway is hindered by this symmetry change, the new transition state will occur at a different crossing, which in turn would lead to large changes in the activation energy as observed experimentall *(3,12)*. This is likely one of the reasons for the modified activation energies of reactions under VSC.

The concentration profile of the equilibrium constant for the dispersion molecular balance shown in Fig. 4D suggests the emergence of collective molecular behavior at the onset of VSC. Similar phase-transition like behavior has already been reported *(15,19)*. Strong coupling of a significant fraction of the molecules at the onset of VSC appears to pull nearly all the molecules into one phase by dipolar interactions due to the zero-point field oscillations of the optical mode. This collective coupling competes with the molecular dynamic disorder inherent in the solution. Nevertheless, the collective phase will affect solvation and solute-solvent interactions, either stabilizing or destabilizing the solute. The observation that VSC reduces the polarity of solvents such as octanol yet induces no change in chemical shifts (Fig. 3B) implies that the polarity change is not to be found at the level of the individual molecule but most likely in the organization of the solvent molecules surrpunding the molecular probe, such as Reichardt's dye *(19)*. The solvent molecules re-organize on a time-scale much faster than that of the NMR measurement. The simplest way to explain a reduction in polarity would be an anti-parallel alignment of the octanol molecules relative to one and other, surrounding the solute dye in the solvation shell which would reduce the macroscopic dipole of the ensemble. Finally, the observed effects of VSC on solvation sensitive processes such as ionic conductivity *(16,17),* self-assembly *(21)* and crystal polymorphism *(20)* are no doubt also related to the emergence of collective behavior and its effect on solute-solvent interactions. For instance, electrochemical experiments show that the modification of ionic conductivity correlates well with changes in hydration and hydration entropies under VSC *(17)*. Recent theoretical studies also point to the role of "polarization" effects where individual molecules are polarized by the collective VSC and fit the current findings, except that they do not induce significant charge redistribution *(44,46)*.

Charge transfer equilibria under VSC can be tilted one way or the other by simply by coupling vibrations of different symmetries *(15)*. In this specific case, one would still expect electronic density redistribution that should be studied by NMR. Nevertheless, the observed changes in the Gibbs free energies in the previous study *(15*) imply that the intermolecular interactions with the solvent and thereby the solvation energies are strongly modified. The emergence of collective behavior under VSC was also observed which may include potentially large changes in entropy *(45)*. Furthermore the entropy of equilibria is itself symmetry dependent *(47)*. Rovibrational averaging is known to affect electronic properties such as chemical shifts and this averaging will no doubt be modified by the formation of hybrid vibropolaritonic modes and may contribute to the effects seen under VSC.

The development of the NMR-compatible cavities allowed us to directly observe the modification of London dispersion forces under VSC with a molecular balance. NMR also provides key insight into the possible mechanisms at play in VSC. The expected VSC induced charge redistribution are so small that they cannot account for the large property changes. Clearly the emergence of collective behavior and the subsequent modification of solute-solvent interactions, together with changes in vibronic coupling and entropy which are symmetry dependent, are at heart of the observed effects of VSC. The ability to observe chemistry under VSC by *in situ* NMR unlocks the study of a variety of chemical systems that would otherwise be inaccessible and should further improve the fundamental understanding of polaritonic chemistry.

AUTHOR INFORMATION

Funding Sources

We acknowledge the support of the International Center for Frontier Research in Chemistry (icFRC, Strasbourg), the Labex NIE projects (ANR-11-LABX-0058 NIE), and CSC (ANR-10-LABX- 0026 CSC) within the Investissement d'Avenir program ANR-10-IDEX-0002-02. M.P. and TS thank the CSC Graduate School funded by the French National Research Agency (CSC-IGS ANR-17-EURE-0016). T.W.E., J.M. and G.R.acknowledge the support of the ERC (project 788482 MOLUSC and 101018894 MetabolismOrigins and 101041933 KI-NET, respectively).

ACKNOWLEDGMENT

The authors are grateful for the advice and support of Michael Ryckelynck and his team, in preparing microfluidic cavities and of Jean-Marie Lehn, Jean-Pierre Kintzinger and Bruno Vincent for their help and advice on NMR experiments. Sinan Bascil is acknowledged for developing a method for sealing the cavities used in this study.

References

(1) K. Nagarajan, T. W. Ebbesen, Chemistry under Vibrational Strong Coupling. *J. Am. Chem. Soc.* **143**, 16877–16889 (2021).

(2) F. J. Garcia-Vidal, C. Ciuti, T. W. Ebbesen, Manipulating Matter by Strong Coupling to Vacuum Fields. *Science* **373**, eabd0336 (2021).

(3) A. Thomas, J. George, A. Shalabney, M. Dryzhakov, S. J. Varma, J. Moran, T. Chervy, X. Zhong, E. Devaux, C. Genet, J. A. Hutchison, T. W. Ebbesen, Ground-State Chemical Reactivity under Vibrational Coupling to the Vacuum Electromagnetic Field. *Angew. Chem.* **55**, 11462-11466 (2016).

(4) W. Ahn, J. F. Triana, F. Recabal, F. Herrera, B. S. Simpkins, Modification of Ground-State Chemical Reactivity via Light–Matter Coherence in Infrared Cavities. *Scienc*, **380**, 1165-1168 (2023).

(5) R. M. A. Vergauwe, A. Thomas, A.; K. Nagarajan, A. Shalabney, J. George, T. Chervy, M. Seidel, M. Seidel; E. Devaux, V. Torbeev, Ebbesen, T. W. Modification of Enzyme Activity by Vibrational Strong Coupling of Water. *Angew. Chem. Int. Ed.* **58**, 15324–15328 (2019).

(6) J. Lather, J. George, Improving Enzyme Catalytic Efficiency by Co-Operative Vibrational Strong Coupling of Water. *J. Phys. Chem. Lett.* **12,** 379–384 (2020).

(7) C. Zhong, S. Hou, X. Zhao, J. Bai, Z. Wang, F. Gao, J. Guo, F. Zhang, Driving DNA Origami Coassembling by Vibrational Strong Coupling in the Dark. *ACS Photonics* **10**, 1618–1623 (2023).

(8) F. Gao, J. Guo, Q. Si, L. Wang, F. Zhang, F. Yang, Modification of ATP Hydrolysis by

Strong Coupling with O−H Stretching Vibration. *ChemPhotoChem* **7**, e202200330 (2023).

(9) G. D. Wiesehan, W. Xiong, Negligible Rate Enhancement from Reported Cooperative Vibrational Strong Coupling Catalysis. *J. Chem. Phys.* **155**, 241103 (2021).

(10) J. Singh, J. Lather, J. George, Solvent Dependence on Cooperative Vibrational Strong Coupling and Cavity Catalysis *ChemPhysChem* **24**, e202300016 (2023).

(11) K. Hirai, H. Ishikawa, Y. Takahashi, J. A. Hutchison, H. Uji-i, Autotuning of Vibrational Strong Coupling for Site-Selective Reactions. *Chem. – Eur. J.* **28**, e202201260 (2022).

(12) A. Thomas, L. Lethuillier-Karl, K. Nagarajan, R. M. A. Vergauwe, J. George, J.; T. Chervy, A. Shalabney, E. Devaux, C. Genet, J. Moran, T. W. Ebbesen, Tilting a Ground-State Reactivity Landscape by Vibrational Strong Coupling. *Science* **363**, 615–619 (2019).

(13) A. Sau, K. Nagarajan; B. Patrahau, L. Lethuillier-Karl, R. M. A. Vergauwe, A. Thomas, A.; J. Moran, J.; C. Genet, T. W. Ebbesen, Modifying Woodward-Hoffmann Stereoselectivity under Vibrational Strong Coupling. *Angew. Chem. Int. Ed.* **60**, 5712–5717 (2020).

(14) J. J. Pietron, K. P. Fears, J. C. Owrutsky, B. S. Simpkins, Electrochemical Modulation of Strong Vibration–Cavity Coupling. *ACS Photonics* **7**, 165–173 (2020).

(15) Y. Pang, A. Thomas, K. Nagarajan, R. M. A. Vergauwe, K. Joseph, B. Patrahau, K. Wang, C. Genet, T. W. Ebbesen, On the Role of Symmetry in Vibrational Strong Coupling Transfer Complexation. *Angew. Chem. Int. Ed.* **59***,* 10436-10440 (2020).

(16) K. Iyoki, T. Fukushima, S. Yoshimitsu, K. Murakoshi, Inherent Promotion of Ionic Conductivity via Collective Vibrational Strong Coupling of Water with the Vacuum Electromagnetic Field. *J. Am. Chem. Soc.* **144**, 12177-12183 (2022).

(17) T. Fukushima, S. Yoshimitsu, K. Murakoshi, Unlimiting Ionic Conduction: Manipulating Hydration Dynamics through Vibrational Strong Coupling of Water. *Chem. Sci.* **14**, 11441–11446 (2023).

(18) S. Kumar, S. Biswas, U. Rashid, K. S. Mony, R. M. A. Vergauwe, V. Kaliginedi, A. Thomas, Extraordinary Electrical Conductance of Non-Conducting Polymers Under Vibrational Strong Coupling, arXiv:2303.03777 (accessed 2023-10-29)

(19) M. Piejko, B. Patrahau, K. Joseph, C. Muller, E. Devaux, T. W. Ebbesen, J.Moran, Solvent Polarity under Vibrational Strong Coupling. *J. Am. Chem. Soc.* **145**, 13215–13222 (2023).

(20) K. Hirai K; H. Ishikawa, J. Hutchison T. Chervy, J. A. Hutchison, H. Uji-i, Selective Crystallization via Vibrational Strong Coupling. *Chem. Sci.* **12**, 11986–11994 (2021).

(21) K. Joseph, S. Kushida, E. Smarsly, D. Ihiawakrim, A. Thomas, G. L. Paravicini-Bagliani, K. Nagarajan, R. M. A. Vergauwe, E. Devaux, O. Ersen, U. H. F. Bunz, T. W. Ebbesen, Supramolecular Assembly of Conjugated Polymers under Vibrational Strong Coupling. *Angew. Chem. Int. Ed.* **60**, 19665–19670 (2021).

(22) K. Sandeep, K. Sandeep, K. Joseph, J. Gautier; K. Nagarajan, S. Meleppatt, K. G. Thomas, T. W. Ebbesen, Manipulating the Self-Assembly of Phenyleneethynylenes under Vibrational Strong Coupling. *J. Phys. Chem. Lett.* **13**, 1209–1214 (2022).

(23) G. Stemo, H. Yamada, H. Katsuki, H. Yanagi, Influence of Vibrational Strong Coupling on an Ordered Liquid Crystal. *J. Phys. Chem. B* **126**, 9399–9407 (2022).

(24) J. George, T. Chervy, A. Shalabney, E. Devaux, H. Hiura, C. Genet, T. W. Ebbesen, Multiple Rabi Splittings under Ultrastrong Vibrational Coupling. *Phys. Rev. Lett.* **117**, 153601 (2016).

(25) R. Damari, O. Weinberg, D. Krotkov, N. Demina, K. Akulov, A. Golombek, T. Schwartz, S. Fleischer, Strong Coupling of Collective Intermolecular Vibrations in Organic Materials at Terahertz Frequencies. *Nat. Commun.* **10**, 3248 (2019).

(26) A. D. Wright, J. C. Nelson, M. L. Weichman, Rovibrational Polaritons in Gas-Phase Methane. *J. Am. Chem. Soc.* **145**, 5982–5987 (2023).

(27) A. P. Fidler, L. Chen, A. M. McKillop, M. L. Weichman, Ultrafast Dynamics of CN Radical Reactions with Chloroform Solvent under Vibrational Strong Coupling. *J. Chem. Phys.* **159**, 164302 (2023).

(28) J. Galego, C. Climent, F. J. Garcia-Vidal, J. Feist, Cavity Casimir-Polder Forces and Their Effects in Ground-State Chemical Reactivity. *Phys. Rev. X* **9**, 021057 (2019).

(29) J. P. Philbin, Y. Wang, P. Narang, W. Dou, Chemical Reactions in Imperfect Cavities:

Enhancement, Suppression, and Resonance. *J. Phys. Chem. C* **126**, 14908–14913 (2022).

(30) P.-Y. Yang, J. Cao, Quantum Effects in Chemical Reactions under Polaritonic Vibrational Strong Coupling. *J. Phys. Chem. Lett.* **12**, 9531–9538 (2021).

(31) J. A. Campos-Gonzalez-Angulo, R. F. Ribeiro, J. Yuen-Zhou, Resonant Catalysis of Thermally Activated Chemical Reactions with Vibrational Polaritons. *Nat. Commun.* **10**, 4685 (2019).

(32) S. N. Chowdhury, A. Mandal, P. Huo, Ring Polymer Quantization of the Photon Field in Polariton Chemistry. *J. Chem. Phys.* **154**, 044109 (2021).

(33) J. Sun, O. Vendrell, Suppression and Enhancement of Thermal Chemical Rates in a Cavity. *J. Phys. Chem. Lett.* **13**, 4441–4446 (2022).

(34) A. Mandal, X. Li, P. Huo, Theory of Vibrational Polariton Chemistry in the Collective Coupling Regime. *J. Chem. Phys.* **156** (2022).

(35) X. Li, A. Mandal, P. Huo, Cavity Frequency-Dependent Theory for Vibrational Polariton Chemistry. *Nat. Commun.* **12**, 1315 (2021).

(36) T. E. Li, A. Nitzan, J. E. Subotnik, On the Origin of Ground-State Vacuum-Field Catalysis: Equilibrium Consideration. *J. Chem. Phys.* **152**, 234107 (2020).

(37) L. P. Lindoy, A. Mandal, D. R. Reichman, Quantum Dynamical Effects of Vibrational Strong Coupling in Chemical Reactivity. *Nat. Commun.* **14**, 2733 (2023).

(38) L. P. Lindoy, A. Mandal, D. R. Reichman, Resonant Cavity Modification of Ground-State Chemical Kinetics. *J. Phys. Chem. Lett.* **13**, 6580–6586 (2022).

(39) T. E. Li, J. E. Subotnik, A. Nitzan, Cavity Molecular Dynamics Simulations of Liquid Water under Vibrational Ultrastrong Coupling. *Proc. Natl. Acad. Sci.* **117**, 18324–18331 (2020).

(40) E. W. Fischer, P. Saalfrank, Beyond Cavity Born–Oppenheimer: On Nonadiabatic Coupling and Effective Ground State Hamiltonians in Vibro-Polaritonic Chemistry. *J. Chem. Theory Comput.* **19**, 7215–7229 (2023).

(41) J. Fregoni, F. J. Garcia-Vidal, J. Feist, Theoretical Challenges in Polaritonic Chemistry. *ACS Photonics* **9**, 1096–1107 (2022).

(42) J. M. Schümann, J. P. Wagner, A. K. Eckhardt, H. Quanz, P. R. Schreiner, Intramolecular London Dispersion Interactions Do Not Cancel in Solution. *J. Am. Chem. Soc.* **143**, 41–45 (2021).

(43) J. Cao, E. Pollak, Cavity-Induced Quantum Interference and Collective Interactions in van Der Waals Systems, arXiv:2310.12881 (accessed 2023-10-29).

(44) D. Sidler, T. Schnappinger, A. Obzhirov, M. Ruggenthaler, M. Kowalewski, A. Rubio, Unraveling a Cavity Induced Molecular Polarization Mechanism from Collective Vibrational Strong Coupling, arXiv:2306.06004 (accessed 2023-10-29).

(45) G. D. Scholes, C. A. DelPo, B. Kudisch, Entropy Reorders Polariton States. *J. Phys. Chem. Lett.* **11**, 6389–6395 (2020).

(46) C. Schäfer, J. Fojt, E. Lindgren, P. Erhart, Machine Learning for Polaritonic Chemistry: Accessing Chemical Kinetics, arXiv:2311.09739 (accessed 2023-10-29)

(47) W. F. Bailey, A. S. Monahan, Statistical Effects and the Evaluation of Entropy Differences in Equilibrium Processes. Symmetry Corrections and Entropy of Mixing. *J. Chem. Educ.* **55**, 489 (1978).

Supporting Information

Direct Observation of Polaritonic Chemistry by Nuclear Magnetic Resonance Spectroscopy

B. Patrahau[§], M. Piejko[§], R. Mayer, C. Antheaume, T. Sangchai, G. Ragazzon, A. Jayachandran, E. Devaux, C. Genet, J. Moran*, T. W. Ebbesen*

[§] Equal contribution

University of Strasbourg, CNRS, ISIS & icFRC, 8 allée Gaspard Monge, 67000 Strasbourg, France

Table of Contents

1. Lionix microfluidic chip for NMR spectroscopy

Microfluidic devices for Vibrational Strong Coupling were developed in partnership with LioniX International. The microfluidic chip consists of a bottom substrate in which the microfluidic channel is etched. A thin metal layer is deposited inside the channel. To promote the adhesion of the gold mirror (10 nm) to the surface and prevent delamination during cavity assembly, a 5 nm chromium adhesion layer is used. Subsequently, a metal layer consisting of 200 nm gold and 5 nm chromium is deposited around the microfluidic channel on the entire chip. This outer layer enables the microfluidic chip to be assembled by metal bonding with a second substrate. This second substrate features the inlet and outlet ports of the microfluidic channel, a thin layer the size of the metallic microfluidic channel consisting of 10 nm gold and 5 nm chromium corresponding to the second mirror of the Fabry-Perot cavity, and an outer layer of and an outer layer of 200 nm gold and 5 nm chromium deposited on the entire sample required to assemble the device. Since the distance between the two mirrors cannot be tuned, the microfluidic channel is etched in various thicknesses ranging from 10 to 15 μm.

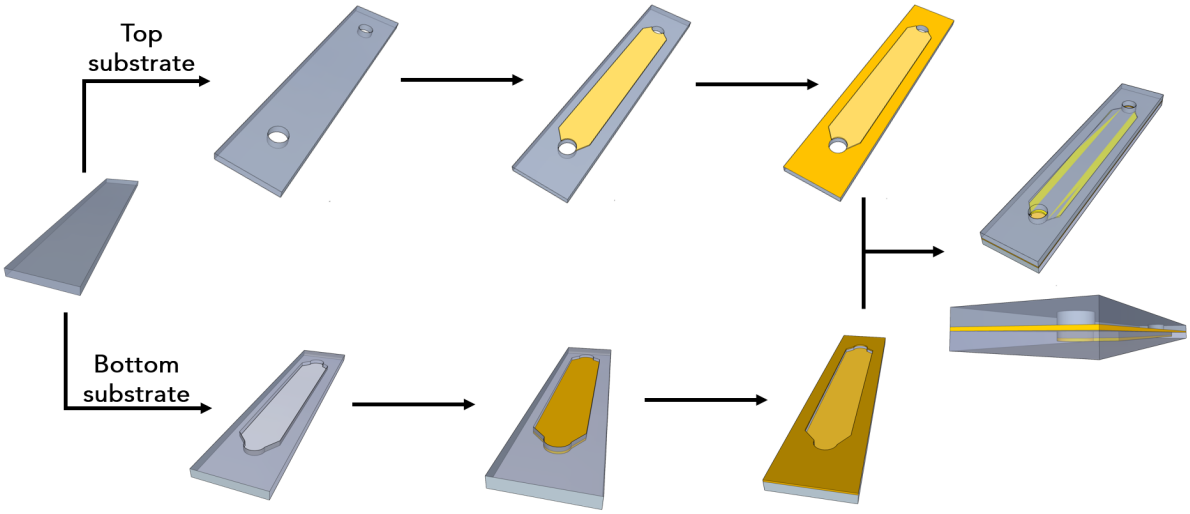

Figure S1. Schematic representation of the fabrication workflow of the microfluidic chip for Vibratonal Strong Coupling.

1. Design of the microfluidic channel

The microfluidic chips are 4 mm wide, 5 cm long and 1 mm thick. The width of the microfluidic channel is 2 mm wide. The depth of the microfluidic channel varies from 10 to 15 μm. The design of the microfluidic channel consists of an inlet and outlet ports with a ∅1.2 mm. The geometry of the microfluidic channel is a straight 4 cm long channel connecting the two inlet/outlet ports. The volume of the sample inside the FP cavity is approximatively 1 μL, depending on the thickness of the channel.

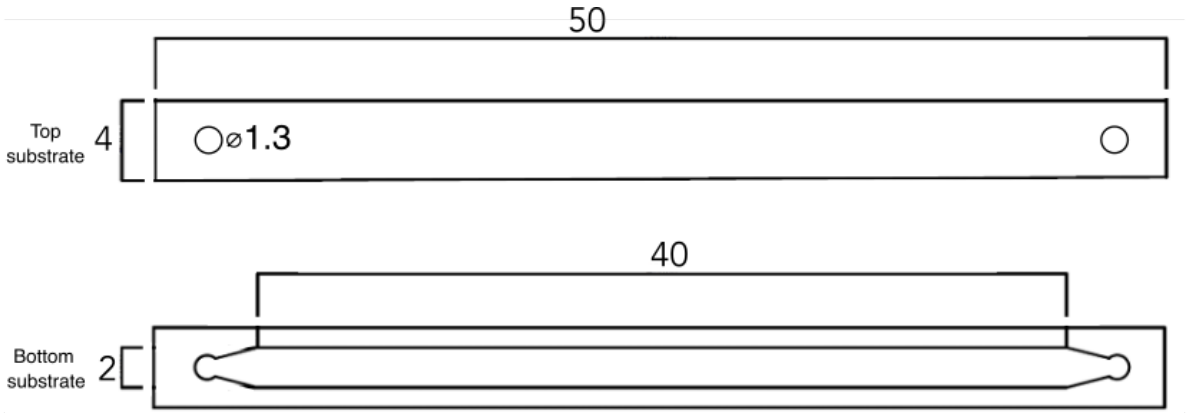

Figure S2. Schematic drawing (in mm) of the microfluidic channel.

2. IR-characterization of fused silica and silicon wafer cavities

The optical properties of the microfluidic Fabry-Perot cavities are characterized using FT-IR spectroscopy in transmission mode, employing a 2 mm x 2 mm aperture. Just like conventional FP cavities, the electromagnetic field is resonant at certain energies (Figure 4). For this microfluidic Fabry-Perot cavity with a thickness of 15 µm, the cavity resonance modes are separated by an FSR of 337 cm^{-1} and have a full

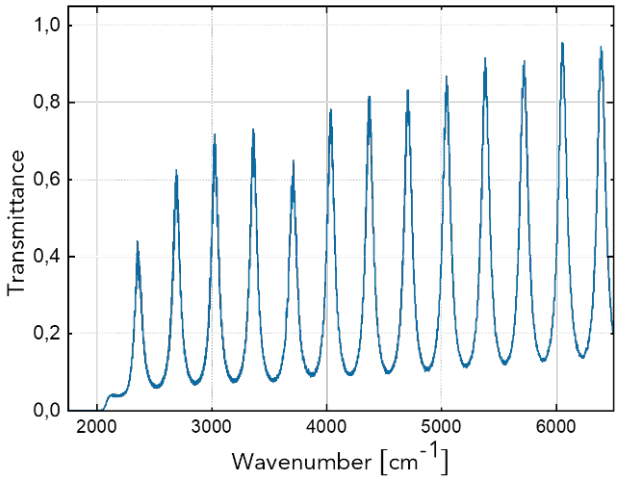

Figure S3. FT-IR spectrum of a microfluidic Fabry-Perot cavity (silica substrate). Due to the absorbance of the substrate the FT-IR spectrum of the cavity is cut-off below 2000 cm^{-1}.

width at half maximum (FWHM) of around 77.0 ± 1.7 cm^{-1} in the region corresponding to vibrational molecular modes (2000 cm^{-1} – 4000 cm^{-1}).

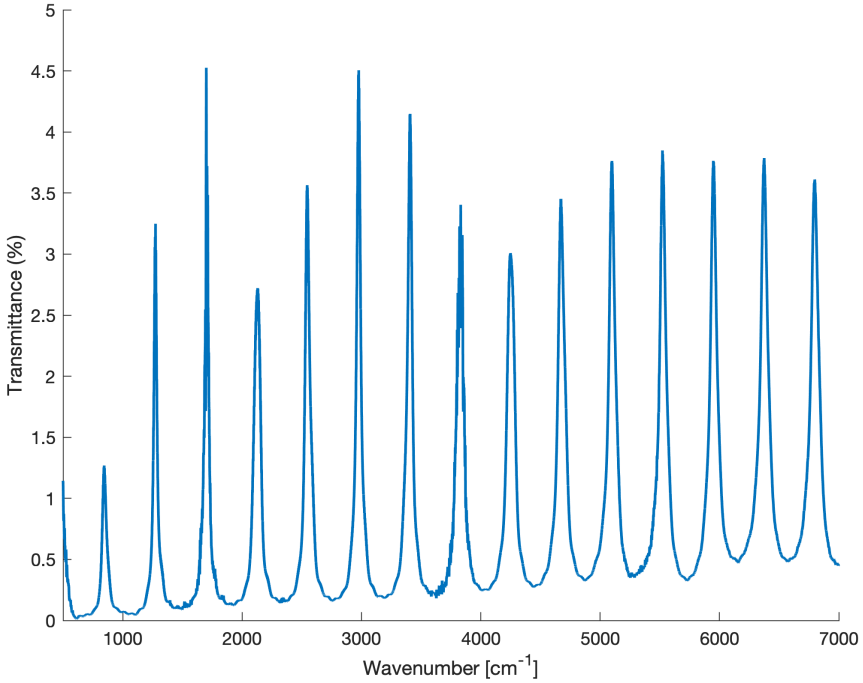

Figure S4. FT-IR spectrum of a microfluidic Fabry-Perot cavity (Si substrate).

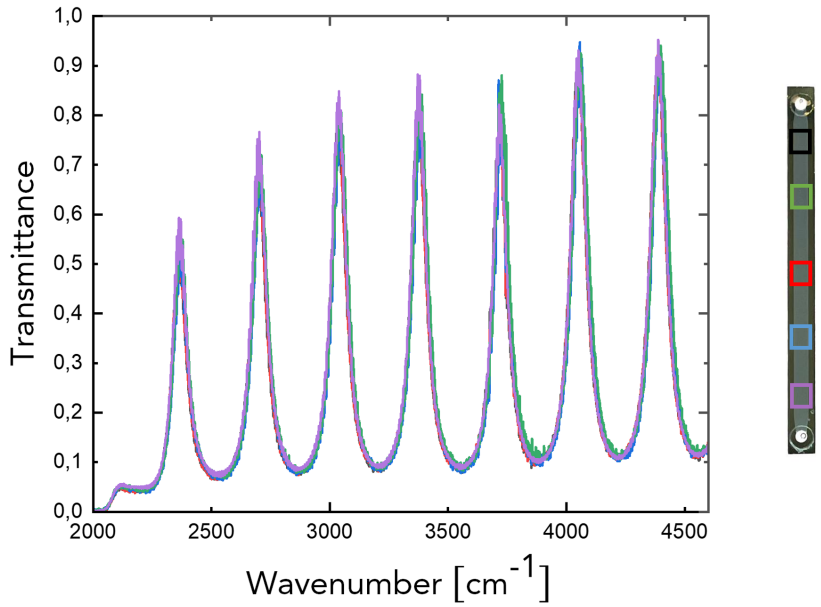

Figure S5. FT-IR transmission spectra of a microfluidic Fabry-Perot cavity measured using a 2 mm x 2 mm aperture along the channel.

Owing to their fixed and consistent pathlength these cavities present a single resonance mode throughout the entire channel, as illustrated in Figure 5, showing the FT-IR spectra measured at various positions along the microfluidic channel.

3. Preparation of cavities for NMR measurements

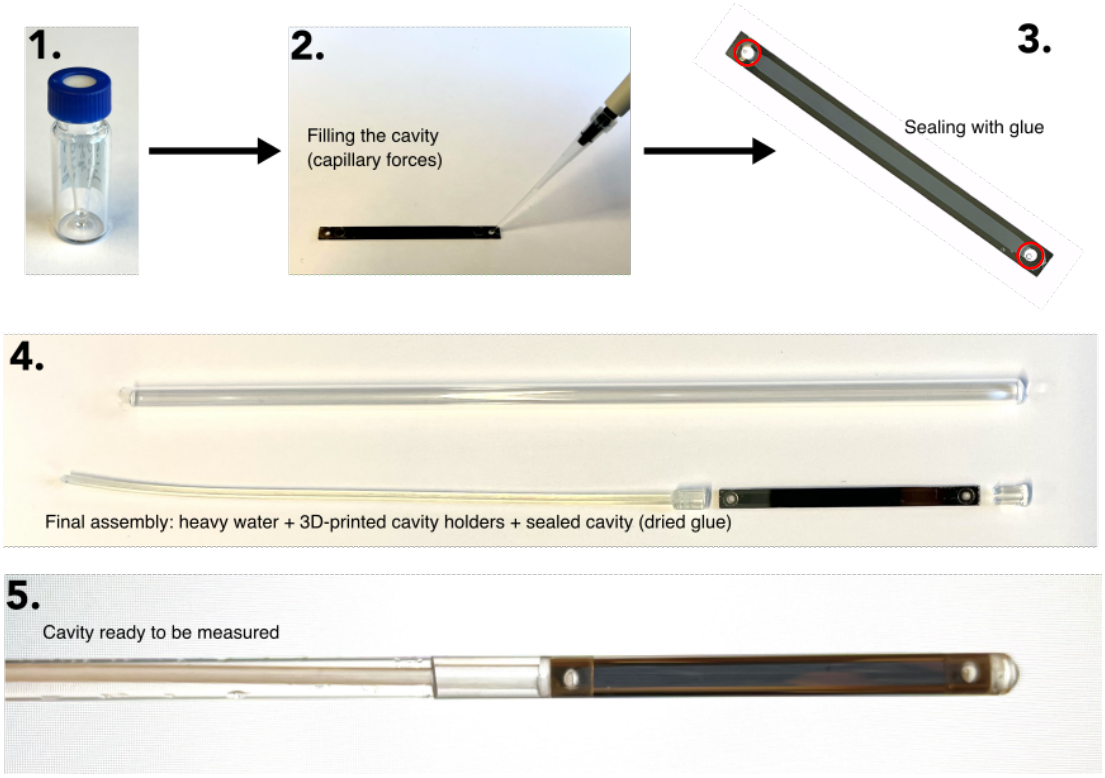

Figure S6. Schematic instructions of cavity preparation.

The following description shows the preparation of a typical cavity setup for NMR measurements. First, a small volume of a solution of the molecular balance was prepared in a 2.0 mL headspace vial with a glass insert to avoid losses. Around 2 μL of the solution were pipetted into one of the cavity inlets, and the solution was allowed to flow through the cavity by capillary forces. Once the channel of the flow cell was fully filled, a small excess of solution was pipetted into the other inlet to fully cover the empty volume, which is necessary to avoid the formation of air bubbles inside the channel once it is tilted. Then, a round microscope glass slide (∅ 3 mm, 0.15 ± 0.02 mm thickness, purchased from AliExpress) was slid on top of both inlets, carefully avoiding trapping of air. A small excess of solution on both inlets (see step before) is necessary in order to stick the glass slide to the cavity with adhesion forces. Lastly, a small amount of cyanoacrylate-based glue ("Superglue") was applied on top and around both glass slides (holding the glass slide with a needle can help to avoid movement during sealing). In our experience, it takes around 20 min for the glue to dry. This ensures sealing of the cavity (in cases where the glue partially entered under the glass slide, only incomplete sealing was achieved, and care must be taken at this step). The cavity was left at RT (23 ± 1°C) for 24 h to equilibrate, as it was reported before that compound **1** requires several hours to reach the equilibrium population due to a high interconversion barrier.

From our experience, this method of sealing the cavities allowed us to obtain good sealing for up to several days or even weeks before evaporation became noticeable. Subsequently, the cavity was inserted with the help of 3D-printed holders (.stl files for printing are included in the Supplementary Information) into a 5 mm NMR Tube pre-charged with 500 μL of D_2O. (Boro 3.3 ASTM Type 1 Class A glass purchased from Deutero, product reference: D200-5-7 – while the quality of the NMR tube is not of large importance in our case, only NMR tubes with thinner walls allow the cavity to fit inside). In our measurements, some ^1H signals due to the cyanoacrylate-based glue became visible (1-2 ppm) after prolonged standing of the cavity in the NMR tube. The signals, however, do not interfere with the signals of the molecular balance (5-7 ppm). Sometimes signals attributed to the depolymerization of the 3D-printed holders were observed at around 3.65 ppm.

4. NMR measurement

All measurements were performed using Bruker 400 or 500 MHz NMR spectrometers and TopSpin software (probes used: PA BBO 400S1 BBF-H-D-05 Z PLUS and CPP BBO 500S1 BB-H&F-D-05 Z). The temperature was controlled with a Bruker BCU unit and an internal thermocouple calibrated against methanol ("NMR thermometer") before use, and the spectrometer was allowed to equilibrate for 10 minutes. The pre-equilibrated sample was inserted into an NMR spinner. Note that due to the size of the 3D-printed holders, the position of the NMR tube containing the cavity inside the spinner was manually adjusted by a few millimeters to ensure ideal placement within the sample coils (see Figure S7).

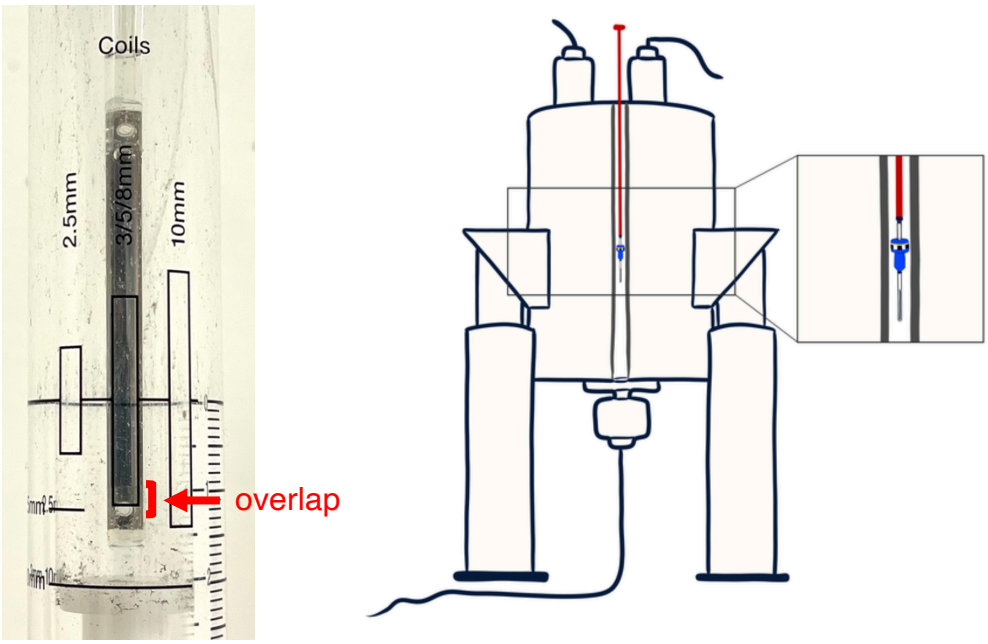

Figure S7. The positioning of the cavity-containing NMR tube inside the depth gauge adjusted to the standard depth (left). This depth should be further corrected by a few millimeters to avoid overlapping with the bottom 3D-printed holder. The NMR tube placed inside the NMR spectrometer (right).

During initial attempts to acquire NMR signals, we observed that the orientation of the cavity inside of the NMR tube relative to the NMR RF pulse is crucial. However, the tube cannot be accurately rotated within the NMR spectrometer with standard hardware. Thus, we constructed a dedicated plastic rod to enable precise orientation of the NMR tube inside the machine. This can be visualized, for example, by measuring the pulse width obtained by using the *pulsecal* command as a function of the angle. The stick is made of 3D-printed parts joined together and is connected to the NMR tube with a standard NMR tube cap. After connecting the tube to the stick, it is placed inside the machine. The next step of the measurement involves locking the field to the signal of D_2O like in a standard NMR measurement.

Figure S8. First authors using the stick to properly orient the cavity inside the NMR spectrometer.

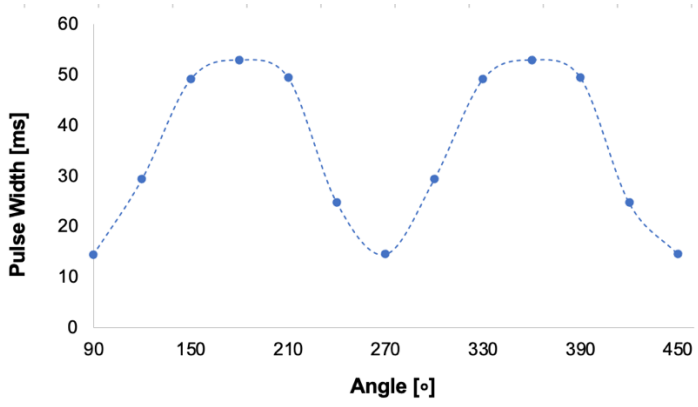

Figure S9. The dependence of pulse width on cavity orientation.

To find the optimal cavity orientation in the spectrometer, the wobb command was executed within the spectrometer, which is normally used to observe the quality of tuning and matching of the spectrometer. While following the impedance curve in

real-time, the NMR tube containing the cavity is rotated using the stick until the resonance frequency of the machine is matched, *i.e.,* the dip of the impedance curve matches with the resonance frequency, as indicated in Figure S10. After manually optimizing the sample orientation in that way, the *atmm* or *atma* commands were executed to further optimize the tuning of the spectrometer.

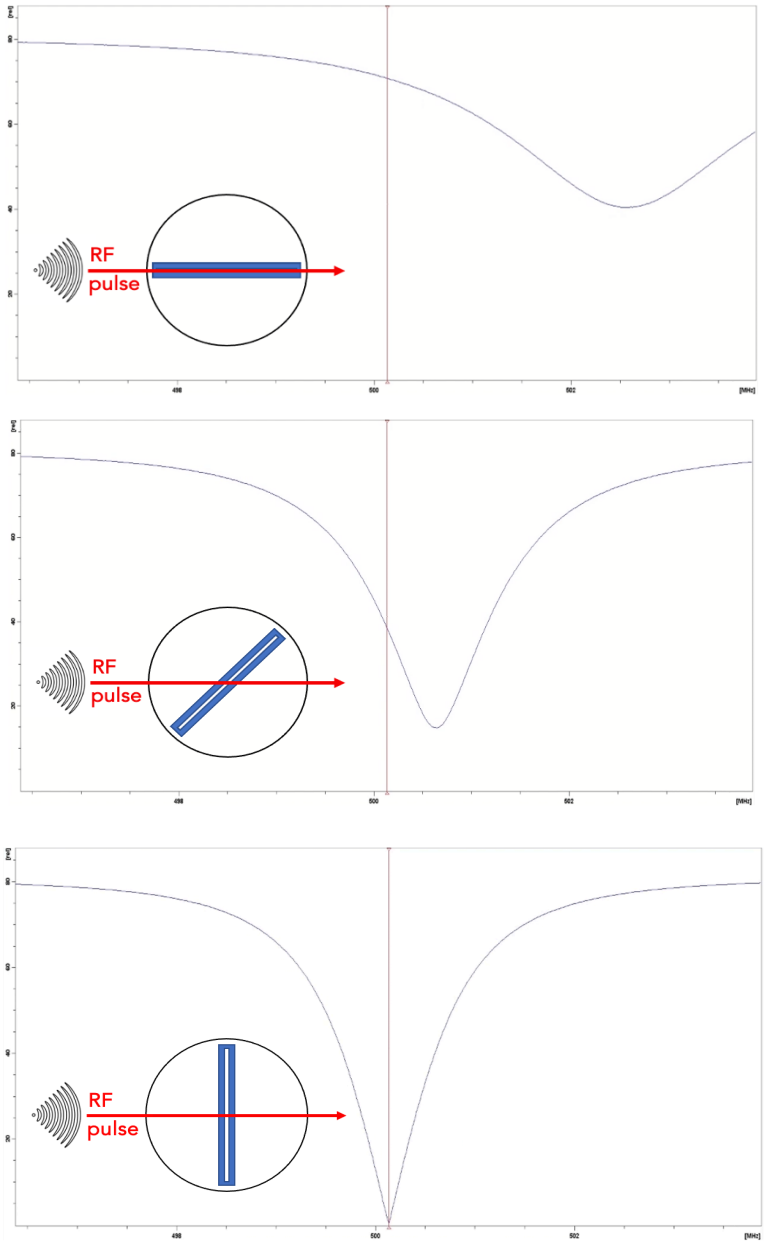

Figure S10. Screenshots of the topshim window with executed *wobb* command used to manually adjust the orientation of the cavity inside of the NMR spectrometer. Orienting the cavity perpendicular to the RF pulse is necessary to match the resonance.

Subsequently, the sample was subjected to routine gradient shimming with additional optimization of the lock signal before (Z-X-Y) and after (Z-X-Y-XZ-YZ-Z).

The quality of shimming greatly depends on the previous settings of shim coils of the machine and sometimes re-shimming might be necessary to improve the quality of spectra.

Next, the receiver gain and pulse width were optimized by executing the *rga* and *pulsecal* commands within topshim. A high value (above 10 ms) of *p1* (pulse width) is an indication of bad sample quality (for example: inhomogeneities like bubbles inside the cavity or suboptimal cavity orientation inside the machine) and we found that a value of 7-10 ms is necessary to achieve sufficient quality (in the case of the 400 MHz spectrometer, PA BBO 400S1 BBF-H-D-05 Z PLUS probe). In order to increase the signal-to-noise ratio of intracavity signals compared to the solvent signal of the water surrounding the cavity, the water peak was suppressed using a standard solvent-suppression pulse sequence (*lc1pngpps*). After that, the acquisition parameters were set, like the number of scans, number of dummy scans, and the relaxation time ($d_1 > 5T_1$ in order to obtain quantitative spectra). Finally, the measurement was commenced by executing the zg command.

To summarize, the overall protocol involves the following steps:

1) Preparing the cavity and equilibrating
2) Placing the cavity inside an NMR tube filled with deuterated water
3) Attaching the rod to the NMR tube
4) Placing the sample inside the NMR spectrometer
5) Locking the field (D_2O)
6) Optimizing the cavity orientation using the rod and atma/atmm commands
7) Shimming
8) Pulse calibration and receiver gain adjustement
9) Quantitative data acquisition ($d_1 > 5T_1$)

5. Cavity NMR spectra

The ^{1}H spectrum below is a representative example of how an NMR spectrum of the studied molecular balance (0.5 M in C_6D_6) inside a Fabry-Perot cavity looks like (path length 15.0 μm, off resonance).

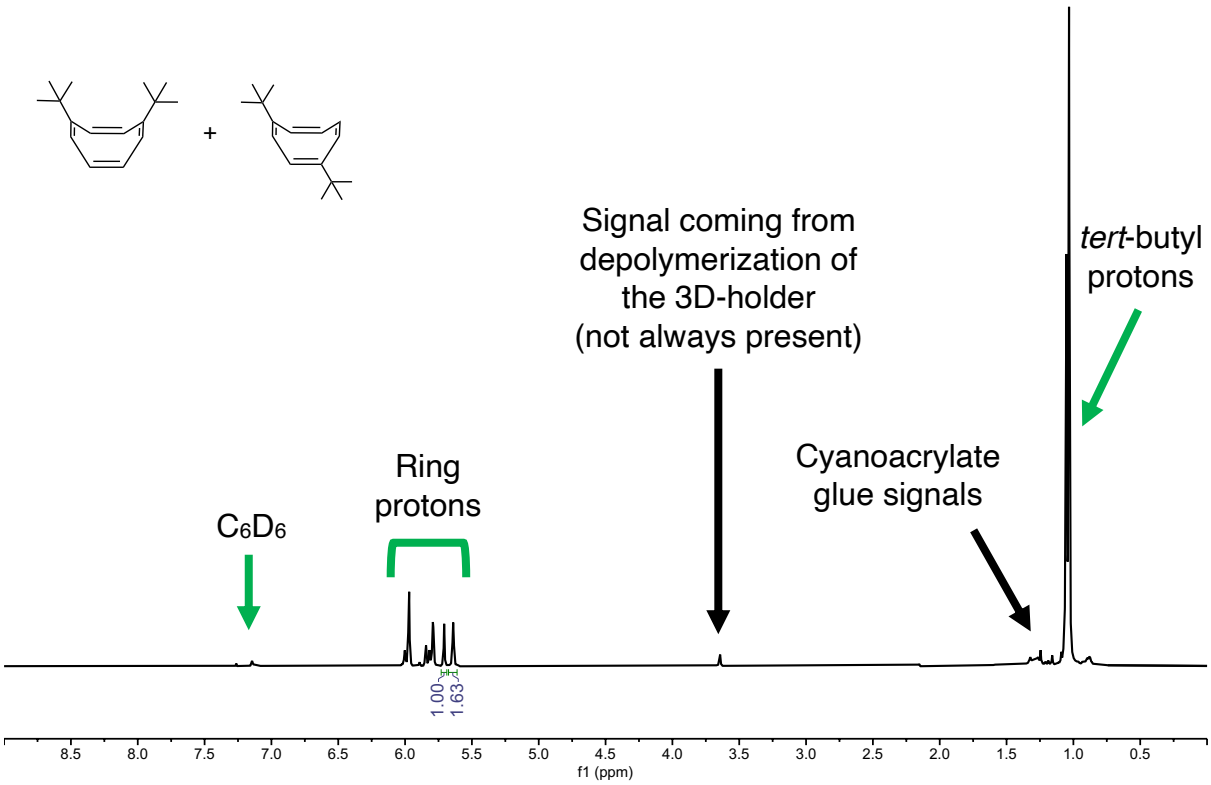

6. Cleaning the microfluidic channel

To remove the sealing, the cavity setup was immersed in acetone to dissolve the glue. After a short time, the glue was wiped off and the glass slide was removed. To assist in the removal of the glass slide, a thin needle proved useful to lever the slide. The insides of the cavity could subsequently be removed by purging with nitrogen or air through one of the inlets, while the other one is immersed in a solvent of choice, which allowed dissolving the intracavity material in the solvent. This step was repeated several times with the cavity being filled again with the same solvent to ensure that all material is recovered, and that the cavity is clean. We obtained the best results using volatile solvents, such as diethyl ether, dichloromethane, or methanol.

7. Synthesis of the Molecular Balance

For the synthesis of X, we largely followed the synthetic route reported by Schreiner at reduced scale [1]. All compounds were purchased from commercial suppliers (SigmaAldrich, TCI, ThermoFisher and abcr) and were used without further purification.

Synthesis of Ershov catalyst

The titanium-bis-catecholate (Ershov catalyst) was synthesized by adding 1.10 g of $TiCl_4$ (5.8 mmol) to a solution of 1.37 g of pyrocatechol dissolved in 8 mL of *m*-xylene. The addition should be performed carefully, as the reaction is exothermic. A brown precipitate forms instantaneously. After the addition, the precipitated product was filtered off (1.2 g of brown solid obtained after drying) and washed thoroughly with *m*-xylene and used without further purification in the next step.

Synthesis of 3,6-di-*t*-butyl-pyrocatechol

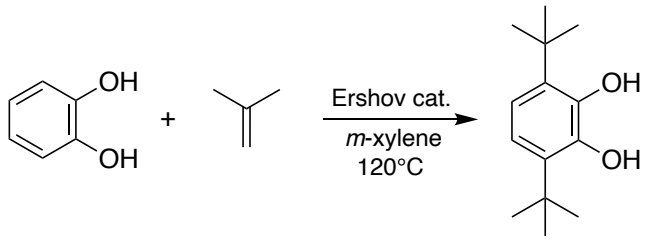

Pyrocatechol (13.75 g, 125 mmol) and Ershov catalyst (0.38 g, 1.0 mmol, 0.1 eq.) were suspended in a 50 mL beaker equipped with a stirring bar in 15 mL *m*-xylene. The beaker with contents was placed in a freezer at -80°C overnight, along with a 50 mL graduate cylinder and a cylinder of isobutene. The beaker was placed in a steel autoclave and liquified isobutene (25 mL, 737 mmol) was added. The autoclave was sealed, and heated to 120 °C, where it was kept for 4 h. Then, the mixture was allowed to cool down to room temperature, and the remaining brown residue was transferred to a round-bottom flask. The residue was subsequently purified by distillation using a Kugelrohr apparatus yielding a liquid that solidified over the course of a few hours to give the product as colorless solid that becomes yellow on standing (18.6 g, 83.7 mmol, 67%).
The analytical data correspond to those reported in the literature. [1]

^{1}H NMR (400 MHz, $CDCl_3$) δ 6.78 (s, 2 H), 5.37 (s, 2 H), 1.42 (s, 18 H).

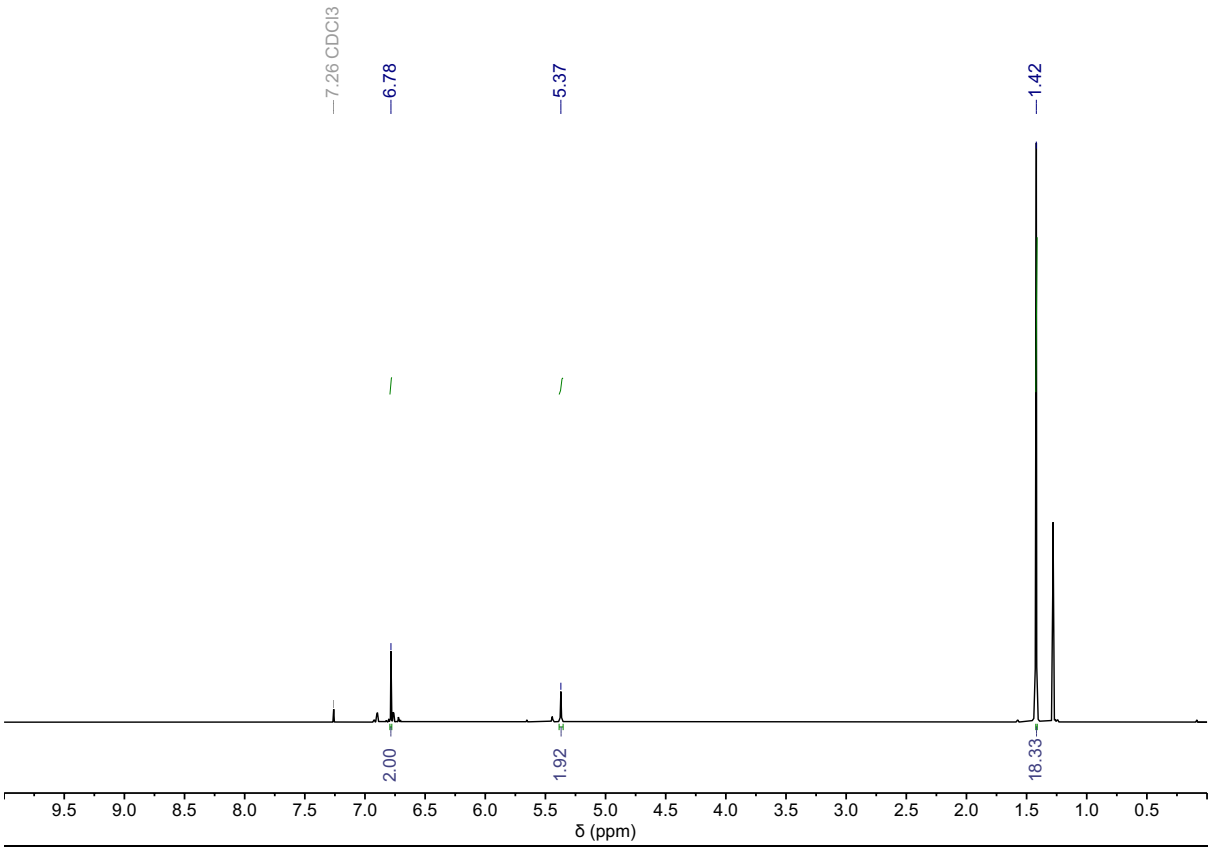

Corey–Suggs oxidation of 3,6–di–t–butyl–pyrocatechol

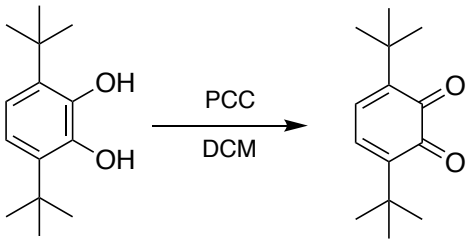

A 100 mL round-bottom flask with a magnetic stirring bar was charged with 3,6-di-*t*-butyl-pyrocatechol (1.9 g, 8.3 mmol) and dissolved in 25 mL of dichloromethane. While stirring, pyridinium chlorochromate (4.1 g, 19.0 mmol, 2.5 eq.) was added at room temperature, causing an immediate color change of the solution to black. After TLC indicated full conversion of the reactant (3 h), the solution was filtered through Celite® and the filtrate was dried over sodium sulfate. After evaporation of the solvent *in vacuo*, the product was obtained as a dark green-brown solid (1.6 g, 7.4 mmol, 90%).

The analytical data correspond to those reported in the literature. [1]

^{1}H NMR (400 MHz, $CDCl_3$) δ 6.77 (s, 2H), 1.23 (s, 18H).

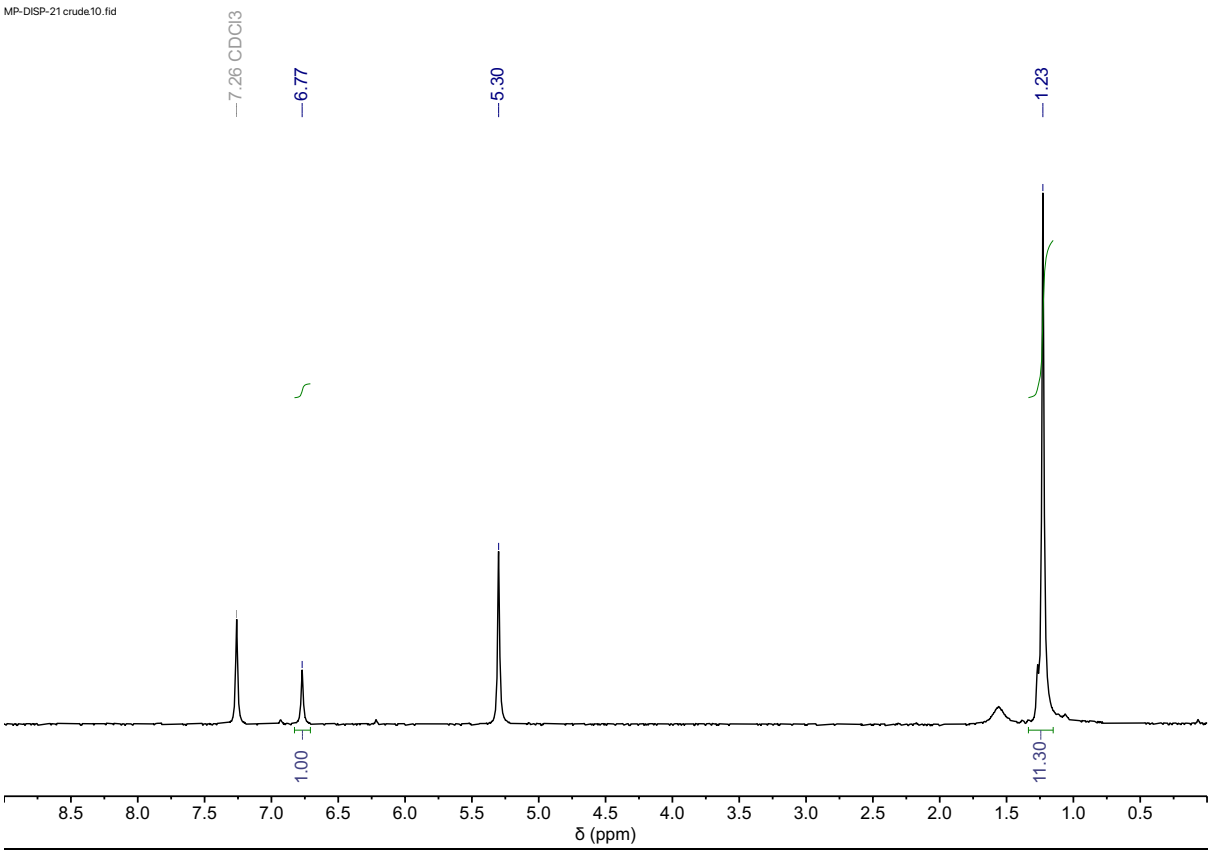

Synthesis of cis-3,4-dichlorocyclobutene

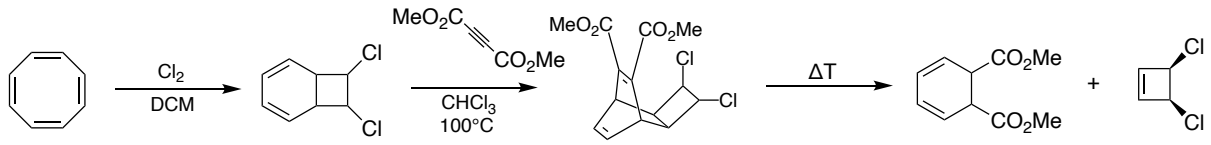

The reported procedure was followed on a reduced scale. We found that 100-fold scale reduction significantly lowers the yield probably due to decomposition (thermal ring opening) occurring during the distillation steps (1.2 g, 3% compared to the reported 49-52g, 40-43%).

The analytical data correspond to those reported in the literature. [1,2]

^{1}H NMR (400 MHz, $CDCl_3$) δ 6.28 (t, J = 1.1 Hz, 1H), 5.15 (t, J = 1.2 Hz, 1H).

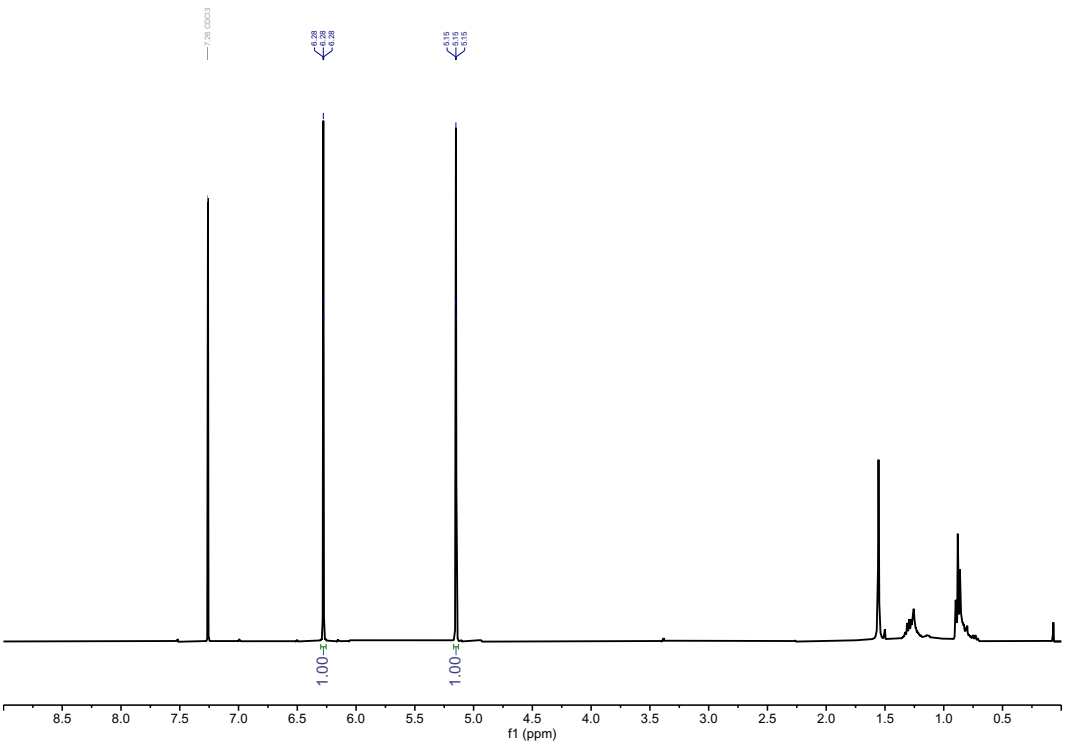

Synthesis of diiron nonacarbonyl

CAUTION: The following procedure must be conducted in a well-ventilated fumehood due to the formation of large amounts of highly toxic carbon monoxide.

For the synthesis of diiron nonacarbonyl we followed the literature procedure at 100 mL scale. [3]

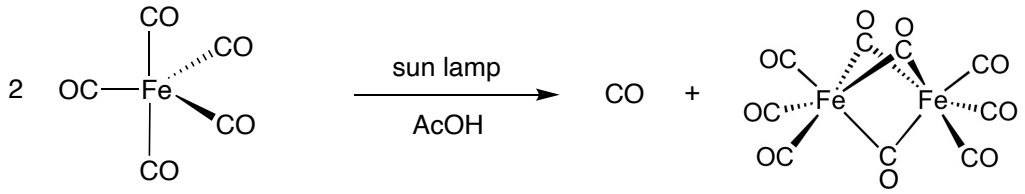

A flame-dried 250 mL round bottom flask equipped with a stirring bar and connected to nitrogen flow with a T-piece was charged with iron pentacarbonyl (100 mL, 146 g, 0.746 mol) and 200 mL of glacial acetic acid. The flask was placed in a Dewar containing acetone and connected to an immersion cooling unit. The setup was placed inside a box covered with aluminum foil and equipped with a sun lamp (OSRAM ULTRA-VITALUX 300W 230V AC). Under stirring and maintaining the temperature at 0 °C, irradiation was performed resulting in the formation of an orange precipitate.

Subsequently, the precipitate was collected by filtration to yield diiron nonacarbonyl as a bright-organce crystalline solid (1.5 g).

Synthesis of cyclobutadieneiron tricarbonyl

CAUTION: The following procedure must be conducted in a well-ventialted fumehood due to the formation of large amounts of highly toxic carbon monoxide.

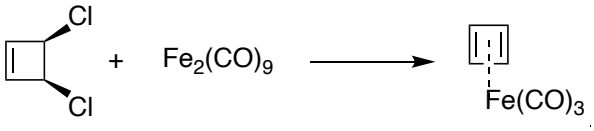

A flame-dried three-necked round-bottom flask equipped with a magnetic stirring bar was charged with cis-3,4-dichlorocyclobutene (1.2 g, 9.8 mmol) and dry benzene (10 mL). The flask was connected to a gas inlet and bubbler, and a consistent flow of nitrogen was activated. While maintaining the temperature at 50 °C and under continuous stirring, small portions of diiron nonacarbonyl (1.5 g in total) were added until no more carbon monoxide evolution was observed. Subsequently, the mixture was cooled to room temperature, was filtered through a plug of aluminium oxide 90 active neutral (activity stage I) and washed with *n*-pentane until the washings were colorless. The crude product was purified by flash chromatography (100% *n*-pentane) to obtain cyclobutadieneiron tricarbonyl (0.97 g, 5.0 mmol, 51%) as a pale-yellow oil.

The analytical data correspond to those reported in the literature. [4] The spectrum below contains residual pentane signals.

^{1}H NMR (400 MHz, $CDCl_3$) δ 3.95 (s, 4H).

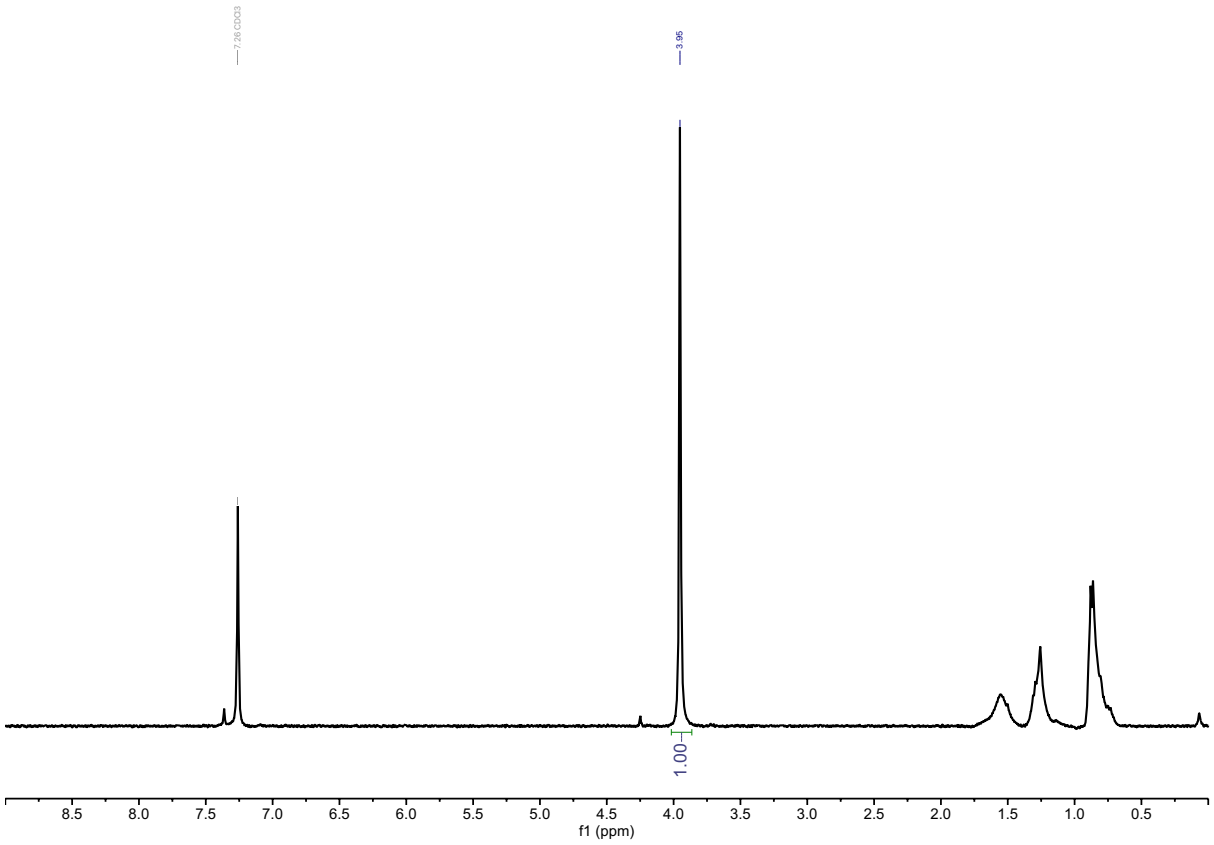

Diels–Alder reaction of 3,6–di–t–butyl–o–benzochinone

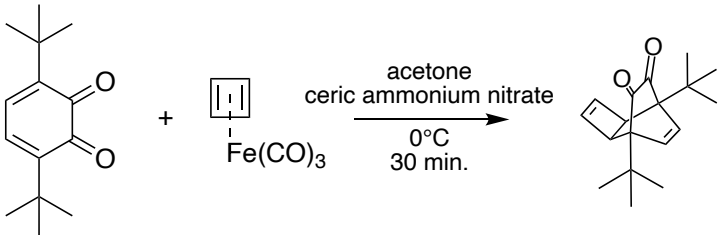

A 100 mL round-bottom flask equipped with a magnetic stirring bar was charged with cyclobutadiene iron tricarbonyl (0.97 g, 5.0 mmol, 1.1 eq.), 3,6-di-*t*-butyl-*o*-benzochinone (1.0 g, 4.6 mmol, 1.0 eq.), and acetone (25 mL). Under stirring, the dark green-brown solution was cooled down to 0 °C and ceric ammonium nitrate (CAN, 5.10 g, 9.30 mmol, 2.0 eq.) was added in small portions over 30 min. Then, the cooling was removed, and the reaction was stirred at ambient temperature until no starting material was detectable by TLC. The solvent was evaporated, the crude product was dissolved in dichloromethane, the solution passed through a plug of Celite® and XX was added until the washings were colorless. Evaporation of the solvent *in vacuo* yielded a brown residue, from which the product was obtained by extraction and subsequent recrystallisation with *n*-hexane yielding 200 mg of crystalline orange solid (0.7 mmol, 16%).

The analytical data correspond to those reported in the literature. [1]

^{1}H NMR (400 MHz, $CDCl_3$) δ 6.26 (s, 2 H), 5.97 (s, 2 H), 3.32 (s, 2 H), 1.10 (s, 18 H).

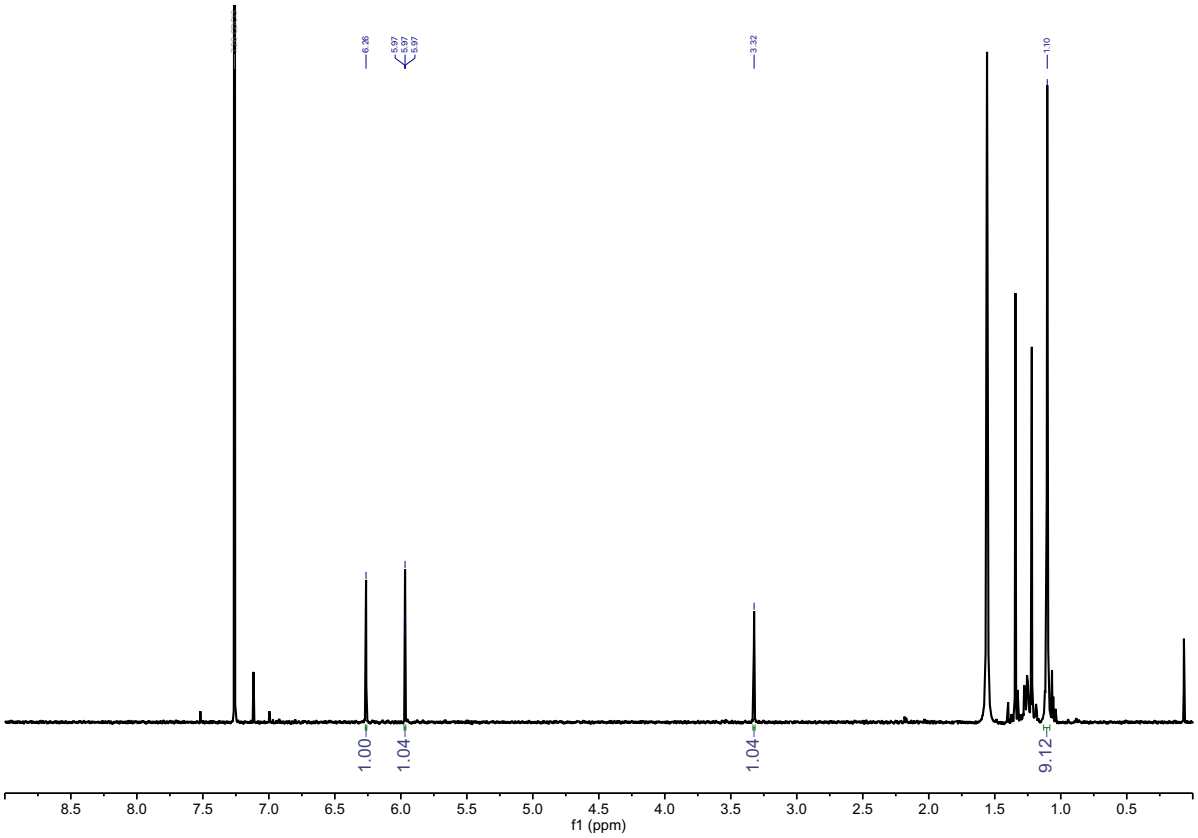

Starting–Zwanenburg photodecarbonylation of 1,6–di–t–butyl tricyclo[4.2.2.00.25]deca–3,7– diene–9,10–dione

For the synthesis of cyclooctatetraene, we utilized a literature procedure from ref. 1 at a reduced scale.

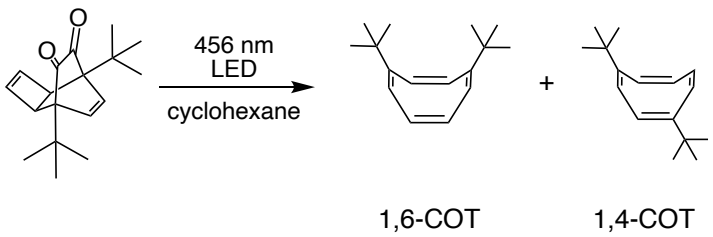

1,6-Di-*t*-butyl-tricyclo[4.2.2.0$^{2.5}$]deca-3,7-diene-9,10-dione (200.0 mg, 0.7 mmol) was suspended in 7 mL of cyclohexane in a glass vial charged with a magnetic stirrer. The vial was closed with a septum pierced with a needle for pressure equilibration. Under stirring, the yellow suspension was irradiated with two 456 nm LEDs (Kessil PR160L, 19V 40W Max) for 16 h. After several minutes, a color change from yellow to dark orange was observed. After 16 h the solution lost most of its color but remained slightly orange. The solution was filtered through a plug of silica, washed with XXX, and the solvent was evaporated *in vacuo* to yield a slightly yellow oil (64 mg, 0.30 mmol, 41%). For preparation of solutions in our study, its density was determined to be 0.85 mg/μL.

The analytical data correspond to those reported in the literature. [1]

^{1}H NMR (400 MHz, $CDCl_3$) δ 6.05 (s, 2H, 1,6-COT), 6.04 – 6.00 (m, 2H, 1,4-COT), 5.91 – 5.87 (m, 2H, 1,4-COT), 5.78 – 5.77 (m, 2H, 1,6-COT), 5.66 (s, 2H, 1,6-COT), 5.63 – 5.62 (m, 2H, 1,4-COT), 1.08 (s, 18H, 1,6-COT), 1.05 (s, 18H, 1,4-COT).
^{13}C NMR (101 MHz, $CDCl_3$) δ 152.7, 150.9, 132.2, 132.1, 131.1, 123.3, 122.8, 77.5, 36.3, 29.9, 29.8.

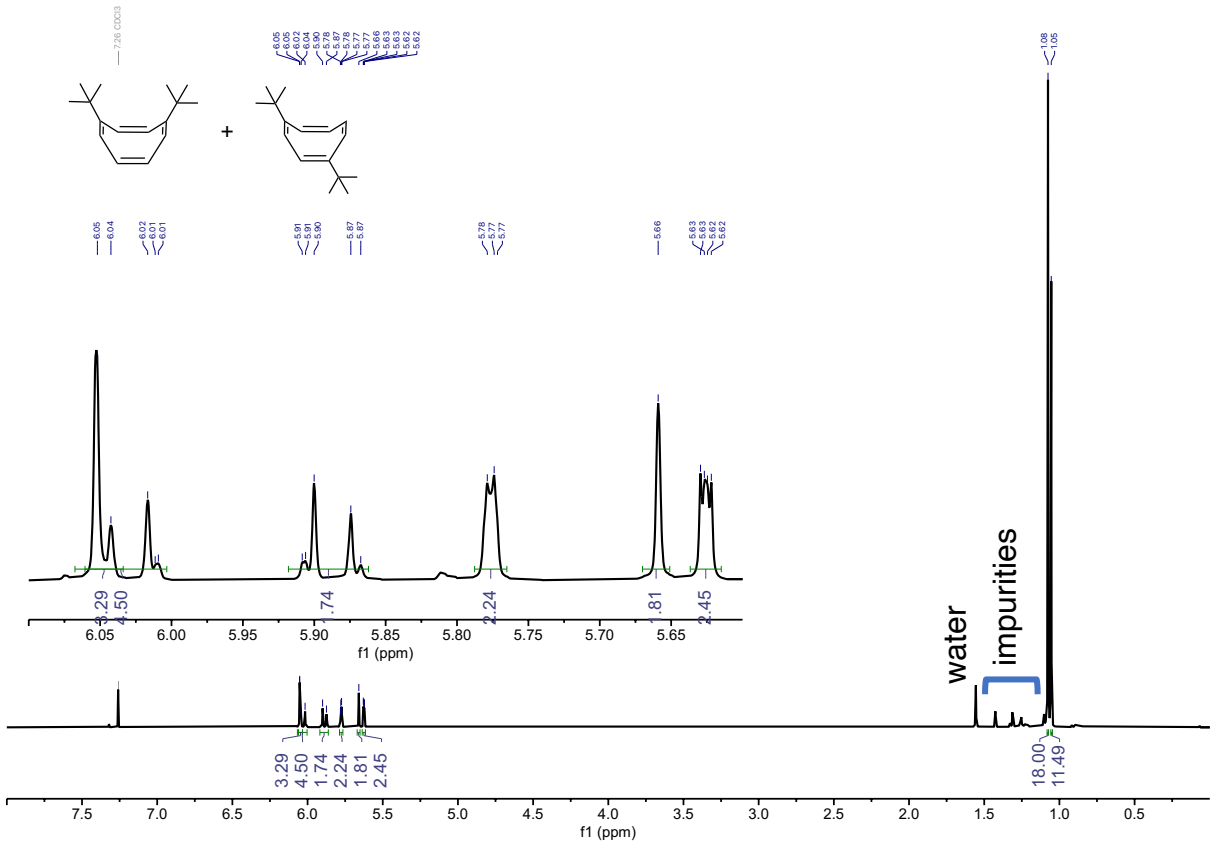

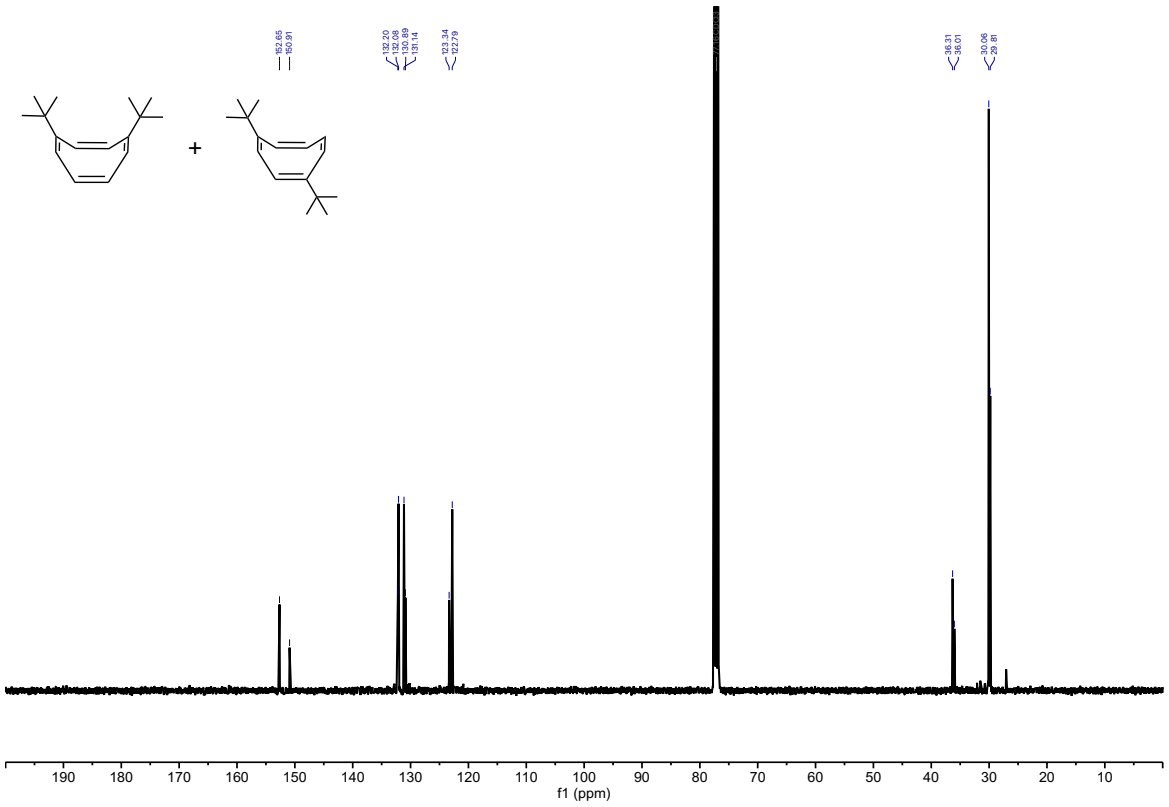

Analysis of the NMR spectrum of the molecular balance at equilibrium

A 22 mM solution of the molecular balance in deuterated benzene was prepared inside an NMR tube (2.6 μL of X dissolved in 450 μL of benzene) and equilibrated for 24 h at 298 K. The value of the equilibrium constant at the given temperature in benzene is in agreement with the value extrapolated from the variable temperature measurements in ref. 1 (1.63).

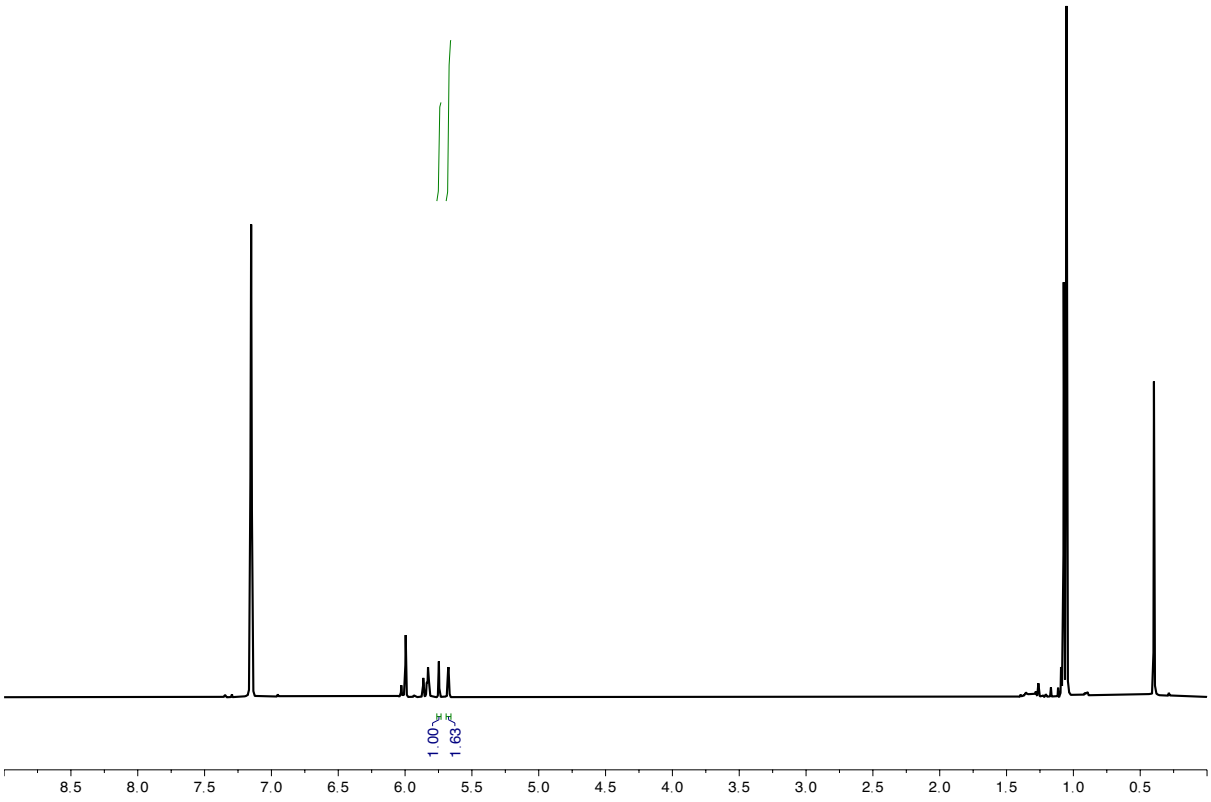

8. IR spectra of cavities coupled and uncoupled to the C–H stretching vibration of the molecular balance

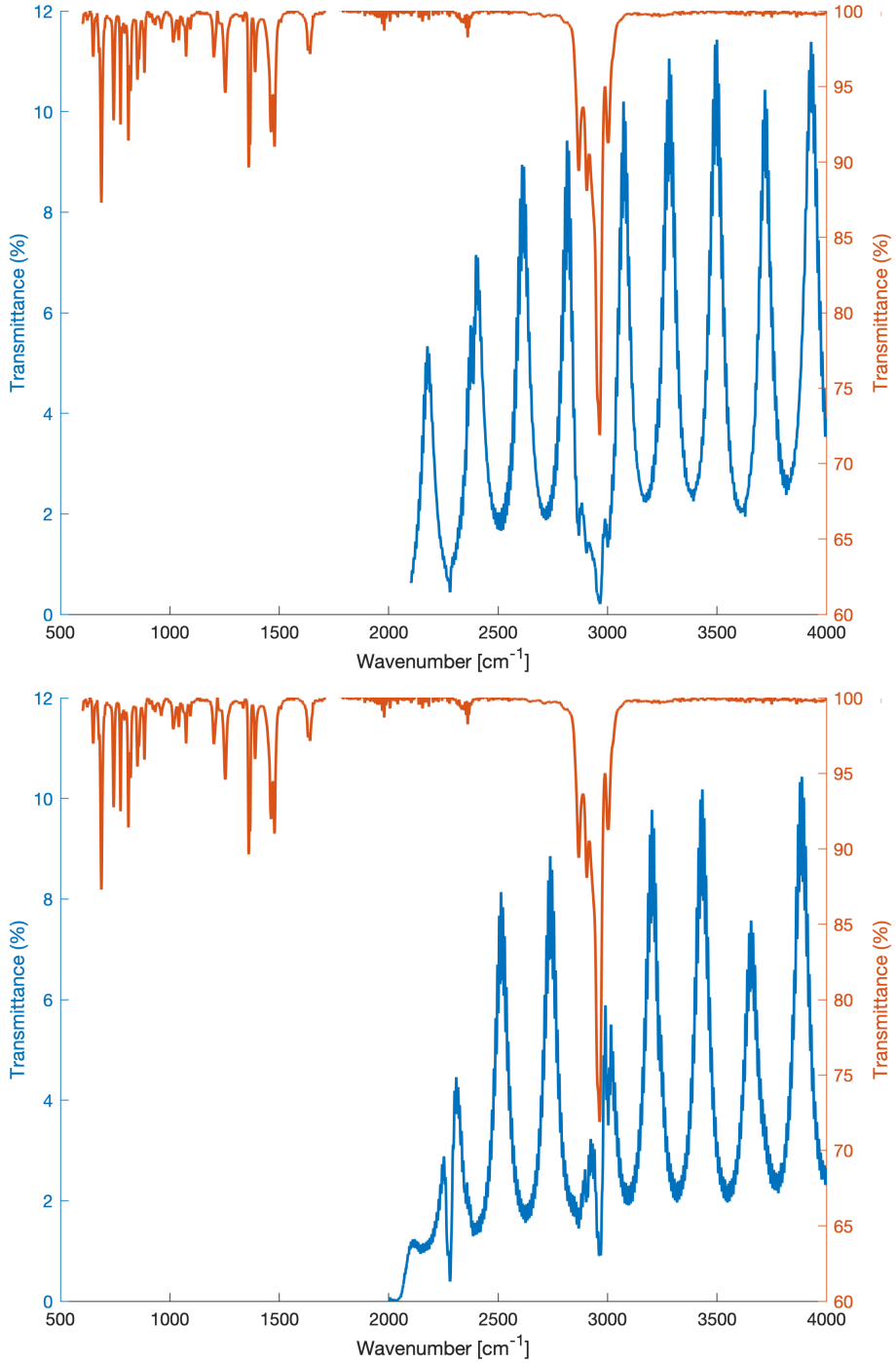

Figure S11. FTIR spectra of the molecular balance (orange) in a cavity on-resonance (up) and off-resonance (down) with the C–H stretch.

9. Measurement of spin-lattice relaxation times (T1)

T1 relaxation times of the relevant proton signals of the molecular balance in C_6D_6 necessary to perform quantitative NMR analysis (qNMR) were determined using the inversion-recovery method (example below, 5 mM concentration).

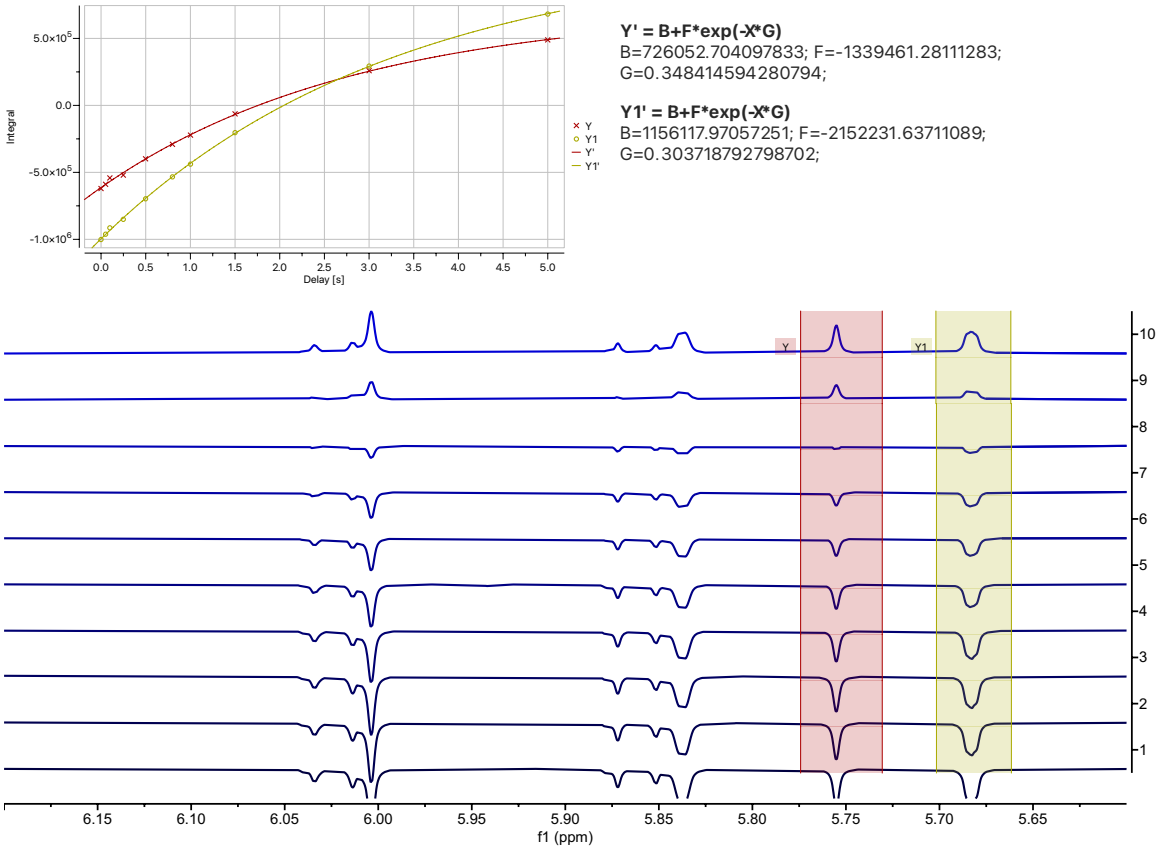

Table S1. Spin-lattice relaxation times (T1) of the molecular balance in 1.5 M solutions in benzene-d_6

Signal	T1 (off resonance cavity)	T1 (on resonance cavity)
5.78 ppm	1.62 ± 0.78	1.75 ± 0.62
5.73 ppm	1.94 ± 0.43	2.17 ± 0.30

10. NMR spectra processing

All NMR spectra were processed in MestReNova 14.3 by first performing automatic phase correction followed by baseline correction (Whittaker Smoother, used with "autodetect" setting). However, we manually modified the settings of "Filter" and "Smooth Factor" to ensure that the peak areas are not altered (see example below).

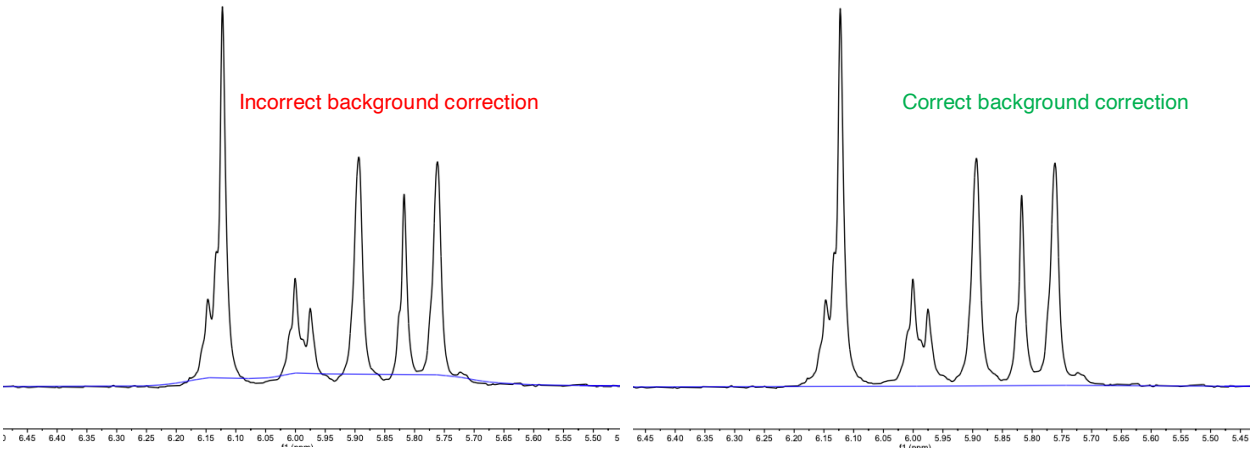

Next, the most downfield signal was referenced to 6.64 ppm to ensure that all spectra are integrated in the same fashion.

11. Equilibrium constant determination

The equilibrium constant (K) for the 1,4-COT/1,6-COT equilibrium was determined by integrating the peak areas for the corresponding protons around 5.75 ppm (1,4-COT) and 5.68 ppm (1,6-COT).

$$K = \frac{Integral_{1,6-COT}}{Integral_{1,4-COT}}$$

Standard error calculation

$$e^K = \frac{\sigma}{\sqrt{N}}$$

where: e^K – equilibrium constant error, σ – standard deviation, N – number of measurements

The standard error for each measured value of equilibrium constant was calculated by dividing the standard deviation of all measurements in each series by the number of measurements.

12. Equilibrium constants in benzene-d_6

Table S2. Equilibrium constants of the molecular balance in 0.1 M solutions in benzene-d_6

Measurement	K (on resonance wafer)
1	1.67
2	1.64
3	1.66
average	**1.66**
standard error	**0.01**

Table S3. Equilibrium constants of the molecular balance in 0.25 M solutions in benzene-d_6

Measurement	K (off resonance wafer)	K (on resonance wafer)
1	1.70	1.66
2	1.72	1.61
3	1.64	1.61
average	**1.69**	**1.63**
standard error	**0.02**	**0.02**

Table S4. Equilibrium constants of the molecular balance in 0.4 M solutions in benzene-d_6

Measurement	K (off resonance wafer)	K (on resonance wafer)
1	1.68	1.65
2	1.61	1.63
3	1.66	1.62
average	**1.65**	**1.63**
standard error	**0.02**	**0.01**

Table S5. Equilibrium constants of the molecular balance in 0.5 M solutions in benzene-d_6

Measurement	K (off resonance wafer)	K (on resonance wafer)
1	1.60	1.31
2	1.62	1.32
3	1.63	1.35
4	-	1.30
5	-	1.32
average	**1.62**	**1.32**
standard error	**0.01**	**0.01**

Table S6. Equilibrium constants of the molecular balance in 1.0 M solutions in benzene-d_6

Measurement	K (off resonance wafer)	K (on resonance wafer)
1	1.62	1.41
2	1.74	1.38
3	1.75	1.41
4	1.57	1.27
5	1.60	1.34
6	1.66	1.18
average	**1.66**	**1.33**
standard error	**0.03**	**0.04**

Table S7. Equilibrium constants of the molecular balance in 2.0 M solutions in benzene-d_6

Measurement	K (off resonance wafer)	K (on resonance wafer)
1	1.66	1.39
2	1.63	1.23
3	1.61	1.43
4	1.63	1.19
average	**1.66**	**1.31**
standard error	**0.03**	**0.03**

References

(1) Schümann, J. M., Wagner, J. P., Eckhardt, A. K., Quanz, H., Schreiner, P. R. *J. Am. Chem. Soc.* **2021**, *143* (1), 41–45.
(2) Cis-3,4-DICHLOROCYCLOBUTENE. *Org. Synth.* **1970**, *50*, 36.
(3) Braye, E. H., Hübel, W., Rausch, M. D., Wallace, T. M. *Inorganic Syntheses* Wiley, **1966**, *8*, 178–181.
(4) CYCLOBUTADIENEIRON TRICARBONYL. *Org. Synth.* **1970**, *50*, 21.